Journal Pre-proofs

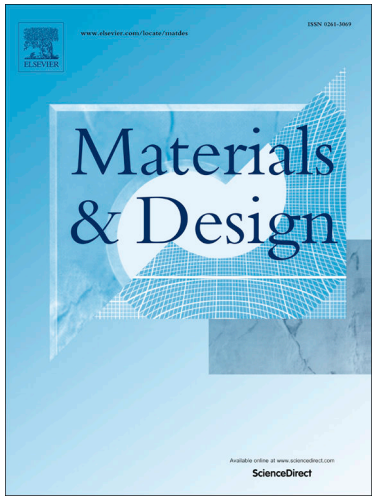

Deprotonated carboxylate-assisted electrospinning of 3D hybrid fiber sponge for rapid hemostasis

Altangerel Amarjargal, Bartlomiej Kalaska, Karol Depczynski, Dorota Kolbuk, Viraj P. Nirwan, Rebecca Hengsbach, Amir Fahmi

PII: S0264-1275(25)01788-5
DOI: https://doi.org/10.1016/j.matdes.2025.115367
Reference: JMADE 115367

To appear in: *Materials & Design*

Received Date: 10 September 2025
Revised Date: 25 November 2025
Accepted Date: 16 December 2025

Please cite this article as: Amarjargal, A., Kalaska, B., Depczynski, K., Kolbuk, D., Nirwan, V.P., Hengsbach, R., Fahmi, A., Deprotonated carboxylate-assisted electrospinning of 3D hybrid fiber sponge for rapid hemostasis, *Materials & Design* (2025), doi: https://doi.org/10.1016/j.matdes.2025.115367

Deprotonated Carboxylate-Assisted Electrospinning of 3D Hybrid Fiber Sponge for Rapid Hemostasis

Altangerel Amarjargal[1,2]*, Bartlomiej Kalaska[3]*, Karol Depczynski[3], Dorota Kolbuk[4], Viraj P. Nirwan[1], Rebecca Hengsbach[1], and Amir Fahmi[1]*

[1]*Faculty of Technology and Bionics, Rhine-Waal University of Applied Science, Marie-Curie-Straße 1, 47533, Kleve, Germany*

[2]*Power Engineering School, Mongolian University of Science and Technology, 8th khoroo, Baga toiruu, Sukhbaatar district, Ulaanbaatar 14191, Mongolia*

[3]*Department of Pharmacodynamics, Medical University of Bialystok, Mickiewicza 2c, 15-089 Bialystok, Poland*

[4]*Institute of Fundamental Technological Research, Polish Academy of Sciences, Pawińskiego 5b, 02-106 Warsaw, Poland*

**Corresponding authors: amarjargal.altangerel@hochschule-rhein-waal.de; amaraa1@must.edu.mn (Altangerel Amarjargal); bartlomiej.kalaska@umb.edu.pl (Bartlomiej Kalaska); Amir.Fahmi@hochschule-rhein-waal.de (Amir Fahmi)*

Abstract

Effective management of non-compressible hemorrhage remains a significant challenge in the field of biomaterials development. Although fluffy fiber sponges with strong hemostatic properties and excellent biocompatibility have been a promising solution, their fabrication has been rather complicated. This study presents a facile in situ deprotonation-induced direct electrospinning approach that enables the fabrication of three-dimensional Gelatin/Eudragit S100 (3D Gel/ES)-based fiber sponges. These sponges are equipped with multiple hemostatic-enhancing moieties to address non-compressible bleeding. The generated 3D sponges exhibit a fluffy texture composed of continuous and interconnected fibers. Results demonstrate a remarkable compressibility, exceptional porosity (>90%), excellent water absorption capabilities (>2000%), very low hemolytic rate (<0.1%), and non-cytotoxic characteristics (cell viability >85%). Furthermore, their hemostatic response has been improved, especially by the incorporation of $CaCO_3$. Consequently, activating the intrinsic pathway of the coagulation cascade, along with the adhesion, enrichment, and activation properties of erythrocytes and platelets. *In vivo* analyses of hybrid fiber sponges confirm their superior hemostatic capabilities compared to traditional gauze and commercial sponge materials. This fabrication strategy is anticipated to open a new avenue for the development of next-generation advanced hemostatic 3D fiber sponge, specifically targeting rapid and effective hemostasis in mild-to-moderate bleeding.

Keywords: 3D hybrid fiber sponges, deprotonated carboxylate, gelatin, electrospinning, Ca^{2+} ions, hemostasis.

1. Introduction

Uncontrollable blood loss resulting from traumatic injuries, surgical interventions, or other forms of bodily harm can pose significant health risks and can even be fatal in severe cases.[1,2] Traditional methods to restore hemostasis after uncontrollable blood loss, such as suturing blood vessels or applying sterile cotton gauze, often fall short when rapid and effective control of hemorrhage is required. Particularly in emergency circumstances where time is of the essence, a delayed action is futile.[3] This challenge underscores the urgent need for the development of advanced hemostatic agents to facilitate quicker blood clotting and minimize blood loss. Ideally, hemostatic solutions should improve performance through efficiency, speed, convenience, and design, be affordable, and lightweight. Thereby broadening their accessibility and usability in medical settings.[4,5] Furthermore, excellent biocompatibility is essential to ensure safe interaction with tissues, while easy degradation without further intervention is crucial for a seamless healing process.[6–8] Over the years, different forms of hemostatic agents composed of both organic and inorganic components, such as particles,[9,10] powders,[11,12] hydrogels,[13,14] sealants,[15,16] nanofibers,[17,18] sponges,[19–21] and foams,[22,23] have been developed. Many of these solutions are already available on the market.[24,25] Each type of hemostatic agent offers distinct advantages over others. However, higher raw material costs, ineffectiveness in managing severe bleeding, and the intricate, multi-step preparation processes limit their wider adoption.

Significant progress has been made recently in the development of nanofiber hemostatic materials. Leveraging their outstanding characteristics, including a high aspect ratio, which enhances interactions with biological systems and facilitates cell adhesion.[26,27] Furthermore, their close resemblance to natural fibrin fibers is crucial in aiding the capture of blood cells, platelets, and various coagulation factors, which are necessary for effective clot formation.[28] Among the vast array of nanofiber materials, functionalized natural or synthetic polymer-based electrospun nanofibers stand out as exceptional candidates for hemostatic membranes.[29,30] Fabricated through the simple electrospinning process,[31–33] these nanofibers possess a unique combination of properties that make them highly effective in promoting blood clotting and wound healing. Their extensive surface area-to-volume ratio significantly boosts their capability to effectively encapsulate and distribute hemostatic bioactive molecules. Intrinsic high porosity and interconnected pores enable rapid blood absorption, thereby expediting the clotting process.[34,35] For instance, Sasmal et al. fabricated electrospun nanofibers encapsulating an antifibrinolytic agent (tranexamic acid) and a chitosan polymer known for its antibacterial and hemostatic properties. The *in vitro* findings highlight the importance of chitosan in promoting hemostasis and establish that tranexamic acid plays a supportive role in the clotting process.[34] Moreover, a recent study has found that gelatin nanofibers infused with calcium ions, which are prepared using the electrospinning technique, exhibit shorter clotting times compared to commercially available hemostatic sponges and gauzes.[29] Nevertheless, the hemostatic electrospun membranes mentioned above possess a two-dimensional (2D) sheet-like configuration composed of densely arranged fiber layers with small thicknesses and inadequate porosity, resulting from the manner in which fibers are deposited during the electrospinning process. This unavoidable characteristic hinders their effectiveness in managing

deep bleeding, irregularly shaped, non-compressible wounds, surgery involving internal organs, and punctured wound hemorrhage.[36]

One of the most effective strategies for managing non-compressible hemorrhage is the use of a sponge-like, porous hemostatic agent with significant blood absorption capability. Additionally, its compressible design allows for necessary conformation and generation of targeted compression at the bleeding site.[17,37] The generation of three-dimensional (3D) electrospun nanofiber sponges represents a significant innovation in developing the next generation of hemostatic materials. The reports on the potential application of such structures for achieving rapid hemostatic action have been somewhat limited till recently.[38,39] One of the reasons could be the challenges and intricacies associated with the fabrication of electrospun 3D nanofiber hemostatic sponges. Although the electrospun 3D fiber sponges have lately been developed for rapid hemostasis, the fabrication method involves a complicated electrospinning setup, necessitating a chamber with controlled humidity, an extra high-voltage generator, and a special collector system.[40,41]

Recently, we demonstrated a cationic polyelectrolyte derived from polymethacrylate-based copolymers as an ideal functional additive for preparing protonated polymer blends. Here, the facile fabrication of fluffy, nanofiber, sponge-like macrostructures via in situ protonation-induced electrospinning was established.[42] The present study introduces a versatile and straightforward approach for the fabrication of anionic 3D fiber sponges without the need for additional electrospinning components to enable fluffy morphology. The induction of 3D morphology was facilitated by the addition of deprotonated carboxylate-equipped anionic polyelectrolyte, resulting in a hybrid fiber sponge composed of Gel/ES containing calcium ions (Ca^{2+}). To enhance the hemostatic effect, inorganic additives, including hydroxyapatite (HA) and $CaCO_3$, were employed as different sources of Ca^{2+}, which are recognized as a coagulation factor IV in the coagulation pathway and are necessary for various stages of the coagulation process.[29] The collective properties of the resulting novel 3D Gel/ES hybrid sponge, functionalized with deprotonated carboxyl groups, were evaluated through comprehensive physicochemical characterizations and compared with those of a pristine 3D sponge. *In vitro* studies of erythrocyte/platelet adhesion, coagulation activation pathways, and whole blood clotting capacity were conducted to evaluate their hemostatic effects. Finally, in this proof-of-concept study, we assessed the hemostatic capacity of 3D hybrid fiber sponges utilizing well-established animal models, specifically the tail amputation and liver injury model in rats. These models were selected for their relevance in simulating real-life injury scenarios, allowing us to evaluate the immediate and effective response of the fabricated sponges in promoting hemostasis.

2. Experimental section

2.1. Materials

Gelatin (Gel, type B with Bloom ~ 225 g), hydroxyapatite, nanopowder with <200 nm particle size (HA, ≥97%), and sodium hydroxide (NaOH) were purchased from Sigma Aldrich. A copolymer based on methyl methacrylate and methacrylic acid, Eudragit® S 100 (ES, Mw = 125,000 g mol^{-1}), was provided by Evonik GmbH (Darmstadt, Germany). Calcium carbonate ($CaCO_3$, 98.5%), methanol (99.9%), and formic acid (FA, 95%) were obtained from Carl Roth. 1, 1, 1, 3, 3, 3-hexafluoro-2-propanol (HFIP, 99 %) was purchased by Fluorochem Ltd. (CHEMPUR).

2.2. Preparation of 3D fiber sponges via deprotonated carboxylate-assisted direct electrospinning.

To carry out direct electrospinning of the 3D fiber sponge, the ES solution was prepared by dissolving ES in alkaline methanol to prepare a deprotonated spinning solution. For comparison, a 2D nanofiber membrane was also fabricated using a 20 wt% ES solution dissolved in methanol/DMF (2:3) binary solvent. To fabricate the 3D Gel/ES-based sponge, two distinct solutions were intended for blend electrospinning. The ES solution was prepared in alkaline methanol, while the Gel was prepared separately by dissolving appropriate amounts in HFIP.

To secure the structural integrity of 3D architecture, we chose a Gel-to-ES blending ratio of 3:2 by weight, as established in our previous research.[32] The resulting blend solution displayed a notably high viscosity with visible phase separation, which could be attributed to the ES solution's highly alkaline nature. To address this issue, several drops of FA were added to the solution (> pH 11). The mixture was then stirred for at least two hours to ensure the formation of a homogeneous solution, which is essential for successful electrospinning. To electrospun hybrid 3D Gel/ES sponges, Gel/ES blend solutions were incorporated with different inorganic additives (HA and $CaCO_3$). Each spinning solution was loaded into a 5 mL syringe with a 21G needle. Electrospinning was performed with the nozzle positioned vertically at room temperature and humidity (22–25 °C and 30–45%, respectively). After electrospinning, the 3D Gel-based nanofiber sponges were subjected to thermal crosslinking in the air at 150 °C for 5 h, rendering them insoluble in water.[40] Table 1 provides details of the sample names, solvents used to dissolve the polymers, and electrospinning parameters.

Table 1. Details of the fiber membrane and sponge materials: composition of the solutions, and parameters of the electrospinning process.

Sample name	Polymer concentration (%, w/w)		Solvent	Inorganic additives (%, w/w)		Flow rate (mL h^{-1})	Tip-to-collector distance (cm)	High voltage (kV)
2D ES	ES	20	methanol/DMF	-		0.6	15	18
3D ES			alkaline methanol (0.6 M NaOH)	-		1	30	16
3D Gel/ES	Gel	15	HFIP	-				
3D Gel/ES-HA	ES			HA	10			

3D Gel/ES-$CaCO_3$	alkaline methanol (0.6 M NaOH)	$CaCO_3$	10

2.3. Characterization

Scanning electron microscopy (SEM). A Jeol JSM-IT100 (Japan/Zeiss, Germany) SEM was used to analyze the morphology of electrospun 2D and 3D fiber samples. Before imaging, the samples were coated with gold using a sputter coater (Cressington Sputter Coater 108 Auto) to enhance the signal-to-noise ratio during the imaging process. The acceleration voltage used in the SEM was between 10-15 kV. Selected magnifications were documented.

Attenuated Total Reflectance (ATR)- Fourier Transform Infrared Spectroscopy (FTIR). Fabricated samples were analyzed with infrared spectroscopy to observe a change in the deprotonation state of the carboxylic group and the presence of functional groups corresponding to various constituents within fiber compositions. The electrospun fibers were pressed on the diamond embedded in the ATR stage of the PerkinElmer Frontier™ spectrometer using a knob fixture. To measure the absorbance in the infrared range, they were scanned from 4000-600 cm^{-1} at a scanning resolution of 2 cm^{-1}.

Thermogravimetric Analysis. The thermal behavior of electrospun fiber samples and their mass degradation properties in response to increasing temperature were characterized using TGA 4000, PerkinElmer. Briefly, ~10 mg of nanofibers were weighed in a ceramic crucible and subjected to controlled temperature increment from 30-700 °C at the rate of 10 °C min^{-1}.

Zeta potential. Zeta potential assessments were conducted using the Malvern Zetasizer NanoS from Malvern Instruments, which is equipped with a HeNe laser (λ= 633 nm) operating at P= 4 mW. A sample weighing 10 mg was ground using a pestle in an agate mortar. The sample was then dispersed in 10 mL of ethanol via ultrasonication. Measurements were taken at 25 °C after allowing for 120 s of equilibration. Three measurements were performed for each sample, with 15 repetitions for each measurement. Cuvettes identified as DTS1070 were utilized.

Evaluation of Porosity and Water Absorption Capacity. The porosity of electrospun 2D and 3D samples was measured following the procedure described in our previous article with slight modifications.[42] Initially, the weight of the pycnometer filled with cyclohexane was recorded as W_1. Subsequently, the dry samples, designated as W_s, were immersed and sonicated for 5 min at 25 °C until the pores were filled with cyclohexane. The pycnometer was then refilled with cyclohexane, and the total weight was recorded as W_2. Finally, following the samples' removal, the residual cyclohexane's weight within the pycnometer was measured and denoted as W_3. All measurements were carried out 3 times, and the porosity of the samples was calculated according to the following equation:

$$Porosity\ (\%) = \frac{W_2 - W_3 - W_s}{W_1 - W_3} \times 100 \qquad (1)$$

To quantitatively evaluate the water absorption capacity, each dry sample was weighed (M_s) and then submerged in deionized (DI) water. At different time points, the samples were retrieved and weighed (M_1). The absorption capacity was calculated according to the following equation:

$$Water\ absorption\ capacity\ (\%) = \frac{W_s - W_1}{W_1} \times 100 \quad (2)$$

Contact angle. The surface wettability of the samples, expressed by the contact angle, was measured on a Goniometer OCA 35 with a tilting unit TBU 90E (DataPhysics Instruments, Germany), attached to a camera iDS UI-3360CP-M-GL R2. Water droplets with a volume of 5 µL were deposited. Average contact angles with standard deviations at various intervals are shown in Figure S1, Supporting Information.

In vitro degradation properties. The in vitro degradation study of the prepared samples was conducted under simulated physiological conditions. Pre-weighed samples (W_s) were immersed in 20 mL of simulated body fluid (SBF, pH 7.4) containing lysozyme (20 U/mL) and shaken at 150 rpm and 37 °C. At 1, 2, 4, 7, 14, and 21 days, the samples were removed, rinsed with deionized water, and dried for weighing (W_1). 3 parallel samples were set up in each group. The relative weight (%) of each sample, both before and after degradation, was determined using the following equation to quantify the degradation

$$Weight\ loss\ rate = \frac{W_s - W_1}{W_1} \quad (3)$$

2.4. Evaluation of biocompatibility

Hemocompatibility. The hemocompatibility of the prepared samples was evaluated using a hemolysis assay, conducted in accordance with our previously published reports, with minor modifications.[28,32] Fresh whole blood from Wistar rats was diluted with PBS in a volume ratio of 1:2. Then, the red blood cells (RBCs) were isolated from plasma using centrifugation at 500x g for 10 min and washed five times with phosphate buffer saline (PBS). Each sample (10 mg) was preheated in 4.5 mL normal saline at 37 °C for 24 h. For the hemolysis test, 0.2 mL of the diluted RBCs suspension (around 5×10^8 cells per mL) was added to 0.8 mL of the above extracts. The RBCs suspension dispersed in PBS was selected as a negative control, and the RBCs suspension dispersed in DI was used as a positive control. All the suspensions were centrifuged at 10,000x g for 3 min after incubating at 37 °C for 1 h. The absorbance of the resulting supernatant was measured at 540 nm using a microplate reader (Synergy HTX, BioTek, Winooski, VT, USA). Four replicates were performed for each group. The hemolysis rate was calculated according to the following equation:

$$Hemolysis\ (\%) = \frac{A_s - A_n}{A_p - A_n} \times 100 \quad (4)$$

where A_s, A_n, and A_p denote the absorbance values of the sample, negative control, and positive control, respectively.

*Cytocompatibility assay***.** Cytocompatibility assessments *in vitro* were conducted using L929 fibroblast cells (Sigma Aldrich). The cells were cultured in a 75 cm² flask containing High Glucose Dulbecco's Modified Eagle's Medium (DMEM) supplemented with 10% fetal bovine serum (FBS) and 1% antibiotics. Incubation was carried out in a 5% CO_2 atmosphere at 37 °C. To detach the cells from the flask, they were first rinsed with PBS, followed by the addition of 5 mL of a 0.05% trypsin solution. The flask was then placed in the incubator for a few minutes. Once the cells were harvested, 10 mL of culture medium was added, and the suspension was centrifuged at room temperature. The resulting pellet was resuspended in fresh culture medium to achieve the desired cell density. Cellular viability studies were performed to evaluate cellular responses to 2D membranes and 3D scaffolds, including cytotoxicity testing on extracts and morphological assessment of the cells.

Cell Viability. Extracts for *in vitro* analysis were obtained by placing 8 mg of each sample in a 24-well plate, following a previously established procedure. In summary, the samples were immersed in 2 mL of culture medium per well and incubated at 37 °C under gentle stirring for 24 h. For reference, wells with and without samples were filled with the same medium. Meanwhile, L929 cells were seeded into a separate 48-well plate, with the number of wells corresponding to the sample extracts plus a control. The cell density was maintained at 1.5×10^4 cells per well, and the plate was incubated for 24 h. After this period, the culture medium in the cell-seeded wells was replaced with undiluted (100%) extracts of each sample. The plate was then returned to the incubator for another 24 h. Subsequently, the extracts were removed, and each well was filled with 180 µL of PBS along with 20 µL of Presto Blue reagent. The plate was incubated again for 60 min before transferring 100 µL from each well to a 96-well plate. Fluorescence was measured using a Fluorescent Accent FL (Thermo Fisher Scientific) with excitation/emission filters set at 530/620 nm. The results were compared to the fluorescence of Presto Blue in blank samples, which exhibited no metabolic activity, and the control (Tissue Culture Plate, TCP), which represented 100% viability. The number of viable cells was determined based on extract studies and calibration curves. The calibration curve was established by cultivating cells on TCP for three days and assessing fluorescence intensity for known cell numbers (2.5, 5, 10, and 20×10^3), measured using a TC20 automated cell counter (Bio-Rad).

Fibroblast Morphology. The morphology of fibroblasts after exposure to 100% extracts was analyzed using fluorescence microscopy. L929 cells were seeded at a density of 20×10^4 cells per well in 400 µL of medium in a 48-well plate. After 24 h, the medium was replaced with extracts, and cultivation continued for another 24 h. Cells were then fixed with 3% formaldehyde for 20 min, followed by treatment with 0.01% Triton X-100 for 5 min to permeabilize the membranes. To visualize the cellular components, nuclei and cytoskeleton were stained for 30 min using a solution containing ActinGreen and NucBlue, which selectively bind to the cytoskeleton and nuclear DNA, respectively. Microscopic images were captured using a Leica AM TIRF MC at 100x and 400x magnification.

2.5. In-vitro hemostatic performance of electrospun 3D fiber sponges

In vitro dynamic whole-blood clotting assay. The dynamic whole-blood clotting assay was employed as described previously with slight modifications.[40] The prepared samples were cut into circles with a diameter of approximately 10 mm, placed in a culture dish, and pre-warmed at 37 °C for 10 min. A volume of 50 µL of sodium citrate anticoagulated rat whole blood was dropped onto the surface of the samples. All the culture dishes were incubated at 37 °C and 50 rpm to allow interaction between the blood and the materials. After 15 min, 10 mL of DI was gently added to release unbound blood without disturbing the clot, and then incubated on a shaker table at 37 °C and 50 rpm for 5 min to collect the free erythrocytes. The control group consisted of citrate-anticoagulated rat whole blood added to 10 mL of DI water. The absorbance of the hemoglobin solution was recorded at 540 nm using a microplate reader (Synergy HTX, BioTek, Winooski, VT, USA). Four replicates were performed for each group. The blood-clotting index (BCI) was calculated according to the following equation:

$$BCI\ (\%) = \frac{A_s}{A_c} \times 100 \qquad (5)$$

where A_s and A_c denote the absorbance values of the sample and control, respectively.

The whole blood clotting time test was assessed according to the previous report with slight modifications.[40] Briefly, 0.5 mL of rat blood (containing 10% sodium citrate) was added to a polypropylene tube containing 5 mg of each sample, followed by 50 μL of $CaCl_2$ (0.20 mol/L). The tube was inverted every 15 s to observe the blood fluidity and record the blood clotting time. The control group consisted of citrate-anticoagulated rat whole blood samples treated identically but without any material added. Four replicates were performed for each group.

RBC and platelet adhesion ability.

The quantitative value of the samples' RBC attachment capability was measured according to a previous study with slight modification.[20] RBC concentrates (200 μL) were added to a polypropylene tube containing 10 mg of each sample. After incubating at 37 °C for 1 h, the sample was rinsed three times with PBS to remove any unattached RBCs. To release hemoglobin, 2 mL of DI water was used to lyse the attached RBCs. Finally, 100 μL of lysed liquid was tested with a multifunctional microplate reader at 562 nm. A mixture of 50 μL RBCs suspension and DI water was used as a reference value for measurement. Five replicates were performed for each group. The percentage of RBCs adhering to the surface was calculated according to the following equation:

$$Percentage\ of\ adhered\ RBC\ (\%) = \frac{A_s}{A_c} \times 100 \qquad (6)$$

where As and Ac denote the absorbance values of the sample and control, respectively.

The adhesion of platelets to the sponges was measured using the lactate dehydrogenase (LDH) assay. First, 5 mg of each sample was placed into 2 mL microtubes and thoroughly wetted with 100 μL of platelet-rich plasma (PRP). The samples were then incubated at 37 °C for 1 h. After incubation, they were washed three times with PBS to remove non-adherent platelets. To lyse the adhered platelets, 1 mL of 1% Triton X-100 in PBS was added, and the mixture was incubated at 37 °C for 1 h. Finally, LDH release was quantified using an LDH assay kit (Sigma-Aldrich, USA) according to the manufacturer's instructions. A microtube containing 100 μL of PRP without any material served as the control. Five replicates were performed for each group. The percentage of platelets adhering to the surface was calculated according to the following equation:

$$Percentage\ of\ adhered\ platlet\ (\%) = \frac{A_s}{A_c} \times 100 \qquad (7)$$

where As and Ac denote the absorbance values of the sample and control, respectively.

SEM analysis of the interaction of 3D Gel/ES-based fiber sponges with platelets/RBCs. Citrate-anticoagulated whole blood collected from rats was centrifuged to obtain PRP and RBC suspension. Samples (1 mg each) were placed in a 24-well plate and incubated with 200 μL of PRP and diluted RBC suspension at 37 °C for 30 min. Subsequently, the samples were thoroughly rinsed with PBS (pH 7.4) and fixed in 2.5% glutaraldehyde in PBS. After fixation, the samples were dehydrated through a graded ethanol series (55%, 65%, 75%, 85%, 95%, and 100%) and then observed under SEM.

In vitro activated partial thromboplastin time (aPTT) and prothrombin time (PT). Fresh sodium citrate-anticoagulated rat blood was centrifuged at 3,500x g for 20 min at 4 °C to obtain platelet-poor plasma (PPP) supernatant. Then, aPTT and PT were automatically determined using an automated coagulation analyzer (Coag Chrom 4000, Bio-Ksel, Poland). Each sample (10 mg) was mixed with PPP (1 mL) and incubated for 30 min at 37 °C. The sample-removed plasma

(50 µL) was mixed with aPTT reagent (Bio-Ksel, Poland) and incubated for 3 min at 37 °C. Subsequently, pre-warmed calcium chloride solution (50 µL, 0.025 mol L^{-1}; Bio-Ksel, Poland) was added to the above mixture, and the time was immediately measured. For the PT assay, the plasma (1 mL) obtained following the above procedure was incubated with samples (10 mg) at 37 °C for 30 min. Immediately after the addition of pre-warmed PT reagent (100 µL; Bio-Ksel, Poland) to the plasma, the time was measured, and the plasma clotting time was recorded as PT. For the aPTT and PT assays, plasma without any added material served as the control. Four replicates of each material were analyzed.

2.6. *In vivo* animal study

All animal studies were approved by the Local Ethical Committee on Animal Testing in Olsztyn, Poland (Permit Number: 07/2025) and conducted in accordance with Directive 2010/63/EU of the European Parliament and of the Council on the protection of animals, the Animal Research: Reporting of In vivo Experiments (ARRIVE) guidelines, and national regulations. Male Wistar rats were obtained from the Centre for Experimental Medicine at the Medical University of Bialystok. The animals were housed under a 12-hour light/dark cycle in a temperature (22 ± 2 °C) and humidity (55 ± 10%) controlled room. They were grouped into cages as appropriate and provided ad libitum access to sterilized tap water and standard chow.

For the liver injury model, twenty rats weighing 180-200 g were randomly divided into gauze, commercial gelatin sponge (Medisponge, Eucare Pharmaceuticals, India), 3D Gel/ES-HA, and 3D Gel/ES-$CaCO_3$ fiber sponge (n = 5 for each group). The rats were anesthetized using isoflurane inhalation at an induction concentration of 4% and a maintenance concentration of 2%. An abdominal incision was made to expose the liver. Before transecting the liver, commercially available sterile gauze pads were placed under the wound to collect blood. A 7.5 mm long and 5 mm deep incision was made in the right lobe of the liver using a scalpel. A 1 cm x 1 cm sample was then applied to the wound. The time taken for bleeding to cease was recorded, along with the total amount of blood lost after the incision. For the tail vein amputation model, twenty rats weighing 180-200 g were randomly divided into the same four groups (n = 5 for each group) and anesthetized as above. After that, 1 cm of each rat's tail was amputated. The tails were then placed on the respective experimental materials. Data on bleeding time and blood loss during the hemostasis process were recorded. At the end of the experiments, all animals were euthanized by exsanguination.

Statistical Analysis

Statistical analysis was performed to assess the significance of the data related to physicochemical characterization, and the biological studies are presented as mean values with standard deviations (SD). Statistical comparisons were conducted using GraphPad Prism 8.0.1 software, with a significance level set at $p < 0.05$. Two-way ANOVA followed by Tukey's multiple comparison test was applied where necessary. Statistical significance was categorized as follows: $p < 0.05$ (*), $p < 0.01$ (**), and $p < 0.001$ (***).

3. Results and Discussion

3.1. Fabrication and morphological analysis of electrospun 2D membrane and 3D sponges

Our recent study has demonstrated that by strategically blending cationic polyelectrolytes with support polymers dissolved in different solvents (non-acidic and acidic), it was possible to obtain a production of array of distinct nanofiber materials, i.e., conventional 2D membranes or advanced 3D sponges.[42] The presence of in situ protonated tertiary amine groups in cationic polyelectrolytes played a key role in the generation of porous 3D nanofiber structures. In the present study, we utilized the in situ deprotonation of anionic polyelectrolyte solutions to electrospun 3D fiber sponges for rapid hemostasis. Consequently, a macroporous fiber sponge containing carboxylate groups is obtained for assisting hemostasis.

Eudragit® S100 (ES) is a synthetic polymer characterized by its pH-responsiveness. It is synthesized from a combination of methyl methacrylate and methacrylic acid in a 1:2 ratio. When electrospinning is performed with ES or a blended solution, it produces a fiber membrane in a 2D sheet-like form, suitable for application in various biomedical fields, especially drug delivery.[43] The electrospun fibers prepared from a methanol/DMF binary solvent system also exhibited a conventional 2D densely packed nanofibrous structure. (Figure 1a).

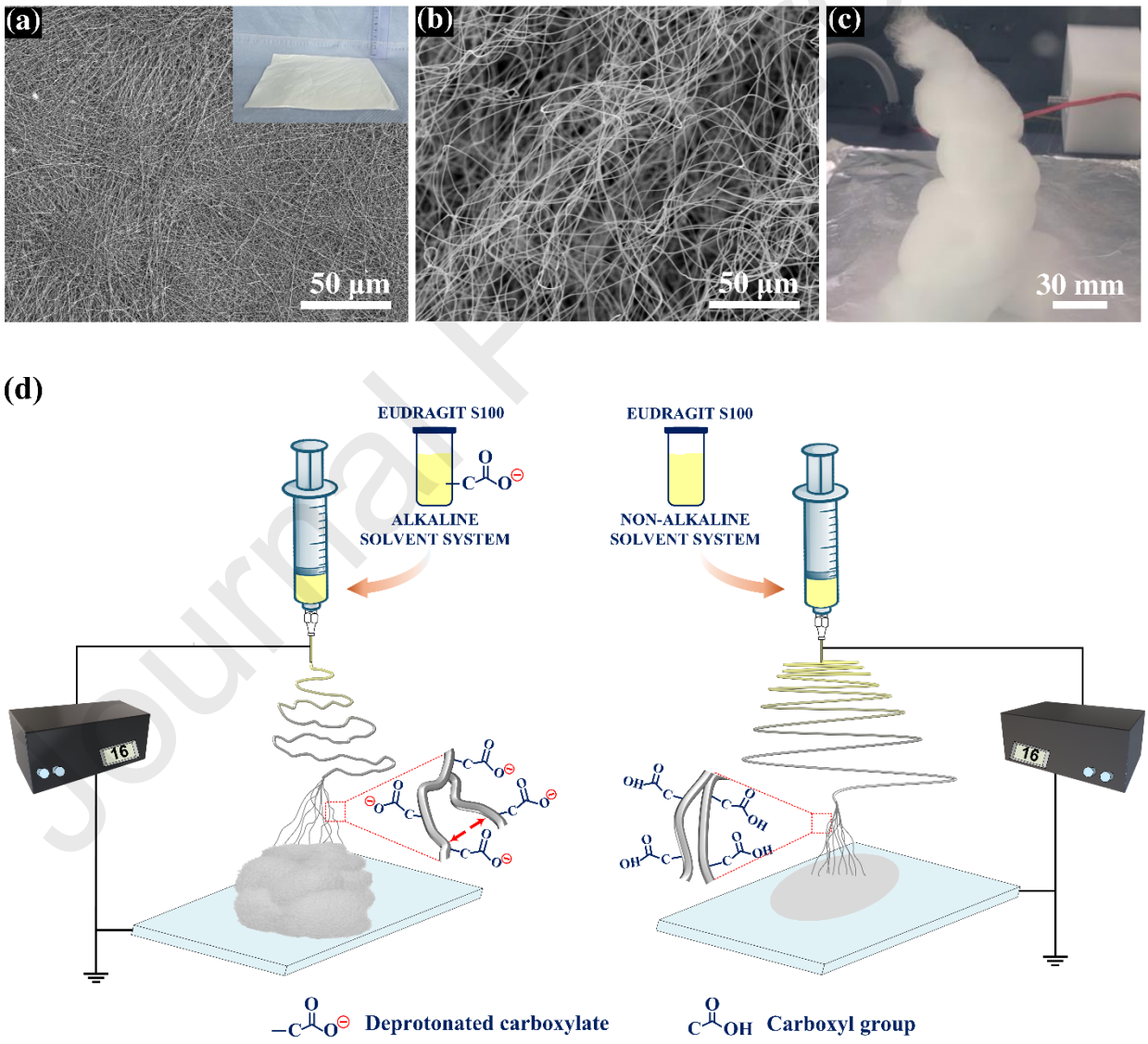

Figure 1. SEM micrographs of the fibers originating from solutions of ES in methanol/DMF with an inset showing a photograph of the resulting 2D membrane (a) and alkaline methanol (b). Photograph of 3D ES fiber sponge (c), and illustration of deprotonated carboxylate-assisted direct electrospinning of 3D ES fiber sponge compared to conventional electrospinning of a 2D ES membrane (d).

By fine-tuning electrospinning parameters to minimize the formation of beaded fibers and encourage the buildup of loosely packed fibers, we successfully produced 3D ES fiber sponges using an alkaline spinning solution (Figure 1b and Movie S1, Supporting Information). The SEM micrograph revealed that the electrospun 3D ES sponge features a distinct arrangement of sparsely distributed fibers about 1 to 3 microns in diameter (Figure 1c). Notably, it exhibits significantly larger pore sizes than the 2D ES nanofiber membrane. In Figure 1d, the differences in 2D and 3D electrospun structures that arise due to the presence of non-deprotonated and deprotonated carboxyl (carboxylate) groups in ES are illustrated. When ES polymer is dissolved in alkaline methanol, the carboxyl groups undergo deprotonation, resulting in an increased density of negatively charged carboxylate groups along the polymer chain. During the electrospinning process, the charged groups are predominantly concentrated on or are present in close proximity to the outer surfaces of the nanofibers.[42,44] Such a distribution of charged groups generates substantial electrostatic repulsive forces between neighboring nanofibers, which play a crucial role in shaping the macrostructure of the resulting materials. As these repulsive forces act upon each fiber, they lead to the deposition of loosely packed fibers, ultimately facilitating the formation of a highly porous 3D architecture. The findings in this study reflect the observations in the previous study, where a similar 3D architecture was generated, albeit using the in situ protonation of tertiary amine groups.

ES is not typically considered a hemostatic material, and to improve its hemostatic performance, 3D Gel/ES fiber sponges were prepared with and without different Ca^{2+} sources. By optimizing the blend ratio of hemostatic biopolymer (gelatin), anionic polyelectrolyte with high charge (Eudragit S100) density, and inorganic additives (HA and $CaCO_3$), an effective 3D fiber sponge capable of enhancing hemostatic response was electrospun. The optical image and SEM analysis provide the macroscopic and microscopic visualization of the prepared 3D Gel/ES and its hybrid fiber sponge with HA and $CaCO_3$, as shown in Figure 2. It is evident from the low magnification SEM micrographs (Figure 2 b, e, and h) that fibers showed a uniform beadless morphology, having highly porous and interconnected pores in all sponges. Figures 2f and 2i show distinctly the successful incorporation of HA and $CaCO_3$, which are integrated into 3D Gel/ES-HA and 3D Gel/ES-$CaCO_3$ fibers, respectively.

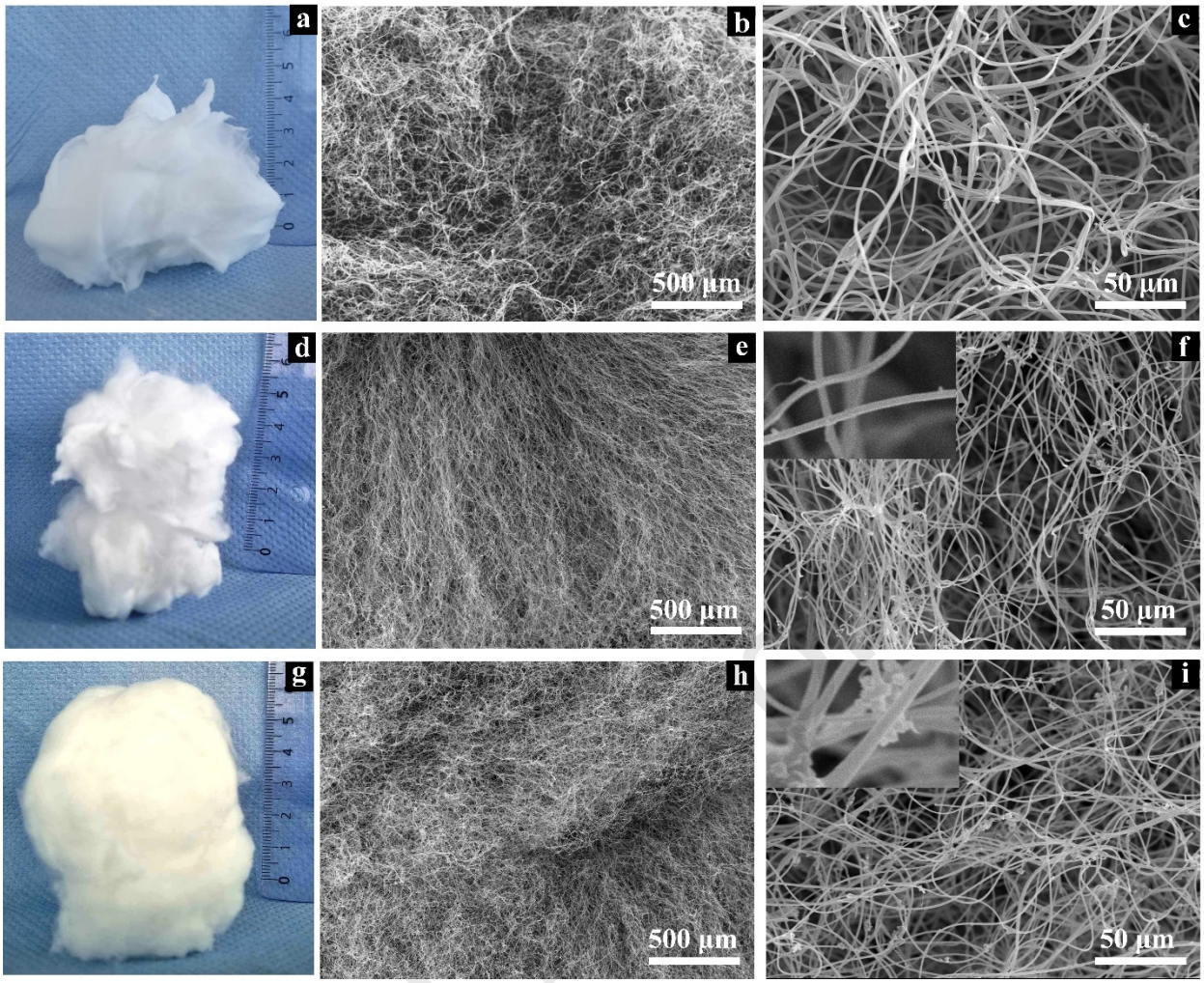

Figure 2. Photographs and SEM micrographs of 3D Gel/ES-based fiber sponges. The left side of the figures shows the photographs of the 3D Gel/ES (a), 3D Gel/ES-HA (d), and 3D Gel/ES-$CaCO_3$ fiber sponges (g). The middle and right sides of the figure show the low- and high-magnification SEM micrographs of the 3D Gel/ES (b and c), 3D Gel/ES-HA (e and f), and 3D Gel/ES-$CaCO_3$ fiber sponges (h and i).

3.2. Physicochemical characteristics

The fabrication of the 3D ES fiber sponge was largely facilitated by the carboxylate functional group in ES. ES polymer was solubilized in an alkaline solution to achieve the deprotonation of carboxylic acid. ATR-FTIR, along with other analyses, was used to verify the presence of carboxylate (COO^-) in the prepared nanofiber sponge. As observed from the absorbance recorded in Figure 3a, the difference in the peak corresponding to the vibration mode of C=O is quite visible. 2D ES nanofibers show a single νC=O vibration absorption peak at 1720 cm^{-1}, whereas the 3D ES nanofibers demonstrate absorption peaks associated with asymmetrical and symmetrical vibration modes of carboxylate (COO^-) at 1680 and 1360 cm^{-1}, respectively.[45–47] The O-H absorbance peaks (~3500 cm^{-1}) derived from carboxylic groups, although varying in intensity, are found within both samples.[47,48] Similarly, other absorbance bands associated with methylene (~2960 cm^{-1}), methyl (~2850 cm^{-1}), and alkene (~1600 cm^{-1}) groups have not changed much between the two types of nanofibers.[49,50] In the fingerprint region, the

absorbance spectrum of 3D nanofibers shows a deforming vibration mode of COO^- at 800 and 725 cm^{-1}.[51,52]

Figure 3b shows the measured infrared spectra of 3D fiber sponges composed of blended Gel and ES, and their further functionalization with HA and $CaCO_3$. Similar to the 3D ES sample, a broad O-H absorbance band (~3350 cm^{-1}) overlapping with an amine absorbance peak associated with gelatin was observed. Further, methyl vibration peaks were observed in all samples along with the carbonyl and alkene vibration bands. Asymmetrical and symmetrical vibration modes of carboxylate were observed in all samples, similar to those of the 3D ES fiber sponge.[45,46] Additionally, the ν_2 vibration absorbance peak (1060 cm^{-1}) due to the presence of tetrahedral PO_4^{3-} could be observed in 3D Gel/ES-HA.[53,54] Contrastingly, two carbonate vibration peaks (845 cm^{-1} (out-of-plane vibration) and 760 cm^{-1} (in-plane vibration)), associated with calcite ($CaCO_3$ polymorph), were observed in the 3D Gel/ES-$CaCO_3$ fiber sponge, confirming the presence of $CaCO_3$.[55] No other significant differences were noticeable from the infrared spectroscopy analysis of the fibers.

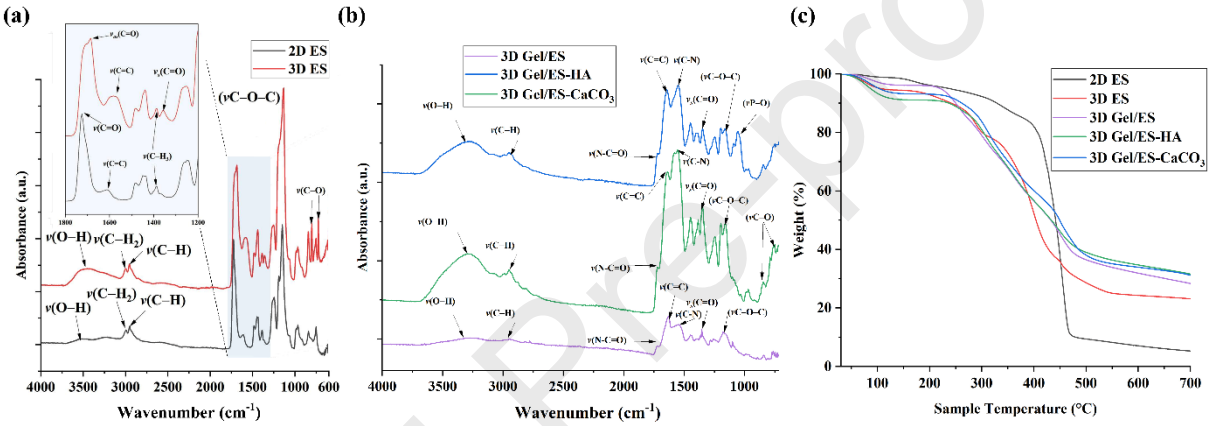

Figure 3. ATR-FTIR spectra of the electrospun materials: Comparison of 2D ES membrane and 3D ES sponge with a close-up view on the carboxylate region. Important regions and peaks are highlighted and labeled (a), and a compilation of spectra of 3D Gel/ES, 3D Gel/ES-HA, and 3D Gel/ES-$CaCO_3$ fiber sponges (b). Thermogravimetric analysis of the electrospun materials with mass loss during heating in comparison to the different fiber compositions (c).

The measured thermal properties of the samples, as well as the differences in their decomposition behavior, can be seen in Figure 3c. All samples show some degree of weight loss during the heating program within the dehydration range. Between 80-100 °C, dehydration-associated weight loss could be observed, especially in 3D fiber sponges. Among the 3D fiber samples, 3D Gel/ES exhibited the maximum dehydration-associated weight loss. All the samples show a multi-step weight loss, presumably due to the presence of multiple components and their oxidation and pyrolysis occurring at different temperature ranges. [56,57] The effect is quite prominent in the 3D Gel/ES fiber sponges, showing multiple steps after the degradation onset temperature. The 2D ES fiber membrane has the highest onset temperature at 422 °C, compared to the 3D Gel/ES, which has the lowest onset temperature at 242 °C. Inclusion of gelatin in nanofibers lowered their decomposition temperatures. However, with the addition of inorganic particles, the onset temperature rose again slightly. [58,59] The exact onset, end temperatures, and weight loss values are presented in Table S1, Supporting Information. There was a reduction in total weight loss at the end of the temperature program with the addition of inorganic particles to the fibers. The changes in compactness of fiber sponges seem to play a role in governing the transfer of heat within the sponges, which leads to varying thermal

behavior. 2D ES fiber samples, being more compact than 3D fibers, can dissipate thermal energy marginally better.[60]

The collective properties that can enhance the hemostatic performance of pristine and inorganic particle-functionalized 3D Gel/ES fiber sponges, including porosity, water absorption ratio, and surface charge potential, were evaluated and compared with a 3D ES sponge and a 2D ES fiber membrane. Figure 4a shows the porosity of different fiber samples. Compared to conventional 2D ES membranes, which consist of densely packed fibers with only surface-level pores, all 3D fiber sponges exhibited over 93% porosity due to their fluffy macrostructure, formed by loosely packed fiber layers that create significantly larger pores in all directions. The increased porosity of the 3D fiber sponge results in a higher specific surface area, which improves its ability to absorb water from the blood and concentrate clotting factors quickly.[39,40] Figure 4b presents a comparative analysis of water absorption capacities between the 2D membrane and the 3D sponges over different periods. The results showed that 3D fiber sponges have an impressive water absorption capacity of over 2000%, thanks to their abundant deprotonated carboxylate functional groups and interconnected, macroporous structure, reaching an absorption level that is 3-4 times greater than that of 2D nanofiber membranes within the initial 30 s. This rapid absorption highlights the sponge's superior hydrophilic properties (inset of Figure 4b and Figure S1, Supporting Information), underscoring the advantages of electrospun 3D structures in the rapid absorption of wound exudate and acceleration of hemostasis. The zeta potential of the prepared samples was assessed to determine their surface charges, as earlier research has established that this potential is one of the essential hemostatic stimulations.[21] The zeta potentials were determined by measuring electrophoretic mobility and, with that, based on ideally spherical shapes. The analysis was helpful in comparing the determined zeta potentials of the samples relative to one another. For the 2D ES sample, a zeta potential of approximately +10 mV is observed. In contrast, all 3D sponges show negative zeta potentials ranging from around -25 mV to around -40 mV. For the 3D fiber samples, the introduction of negative charges by means of deprotonated carboxylate can be concluded (Figure 4c). Consequently, electrostatic repulsion between the fibers, which leads to loosely packed fibers at the macroscale as well as 3D structures seen macroscopically, is indicated. Beneficially, hemostatic responsive materials with a negative zeta potential can activate FXII by absorbing the plasma protein factor XII (FXII). It leads to the initiation of the intrinsic blood coagulation pathway through FXI activation, besides influencing various vascular responses by triggering the plasma contact system.[61,62] Therefore, an effective activation of coagulation factors can be expected from the 3D fiber sponge, particularly 3D Gel/ES-based sponges.

Biomaterials intended for use in the human body must exhibit excellent biodegradability to ensure safe and good integration with biological systems. To demonstrate the biodegradation characteristics of the prepared samples, they were subjected to SBF containing lysozyme for 21 days.[63] As shown in Figure 4d, both the 2D ES membrane and the 3D ES sponge exhibited complete degradation within 1 day. This rapid disintegration can be attributed to the inherent solubility of ES in dissolution media with a pH above 7.[43] Conversely, the weight of 3D Gel/ES-based fiber sponges declined progressively throughout the experimental period, ultimately by over 65%. The comparatively delayed degradation rate observed in the 3D Gel/ES fiber sponges relative to the 2D and 3D ES samples can be attributed to thermal crosslinking. All these findings clearly indicate that the 3D Gel/ES fiber sponges exhibit outstanding biodegradability. In addition to surface properties, structural and mechanical behaviors are another important design consideration for hemostatic performance materials. Especially, sponge-like, porous hemostatic agents are distinguished by their ability to return to their original shape after being compressed. It allows them to effectively cover the entire wound surface and apply the necessary pressure, which aids in achieving hemostasis.[37] When compressed

repeatedly, the fabricated fiber sponge, possessing a distinctive fluffy architecture, can regain its shape, showing good elasticity, as seen in the example of the 3D Gel/ES sponge. (Figure 4e and Movie S2, Supporting Information).

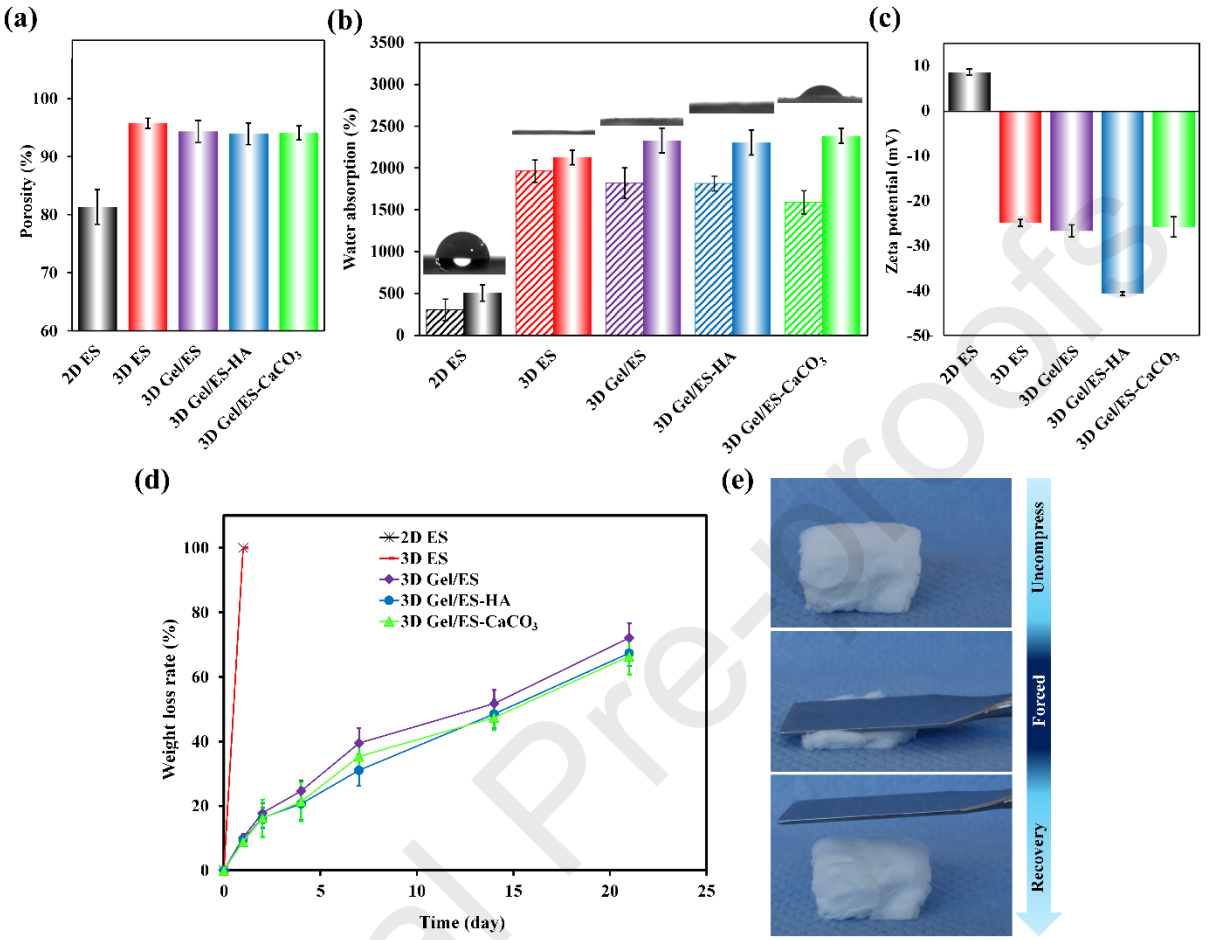

Figure 4. Characterization of electrospun 2D membrane and 3D sponges regarding the porosity (a), water absorption capacity at 30 s (pattern fill) and 180 s (gradient fill) with insets showing water droplets at the samples 30 s after deposit (b), and zeta potential measurements (c), in vitro biodegradation in SBF (d). The 3D Gel/ES fiber sponge can be effortlessly returned to its original state after compression (e).

3.3. *In vitro* hemocompatibility and cytocompatibility

For any new hemostatic material intended for direct contact with wounds, it is crucial that the material presents blood biocompatibility and non-cytotoxic characteristics. According to ISO 10993-4, hemolysis tests are essential for assessing blood compatibility. Hemolysis refers to the process in which erythrocytes break apart, leading to the release of their contents into the plasma. Figure 5a displays the hemolysis rates for each sample group, with PBS serving as the negative control, showing a 0% hemolysis rate, and distilled water serving as the positive control, exhibiting a 100% hemolysis rate. The results showed that the hemolysis rate of all samples was remarkably low, quantified at less than 0.1%, which is well within the acceptable toxicity threshold of 5%. Additionally, the photograph (inset of Figure 5a) indicates that the supernatant for all sample groups, including the negative control, appeared nearly colorless and

transparent. In contrast, the positive control exhibited a bright red coloration. These results confirmed that all the fabricated fiber samples had excellent blood compatibility in the hemolytic assay.

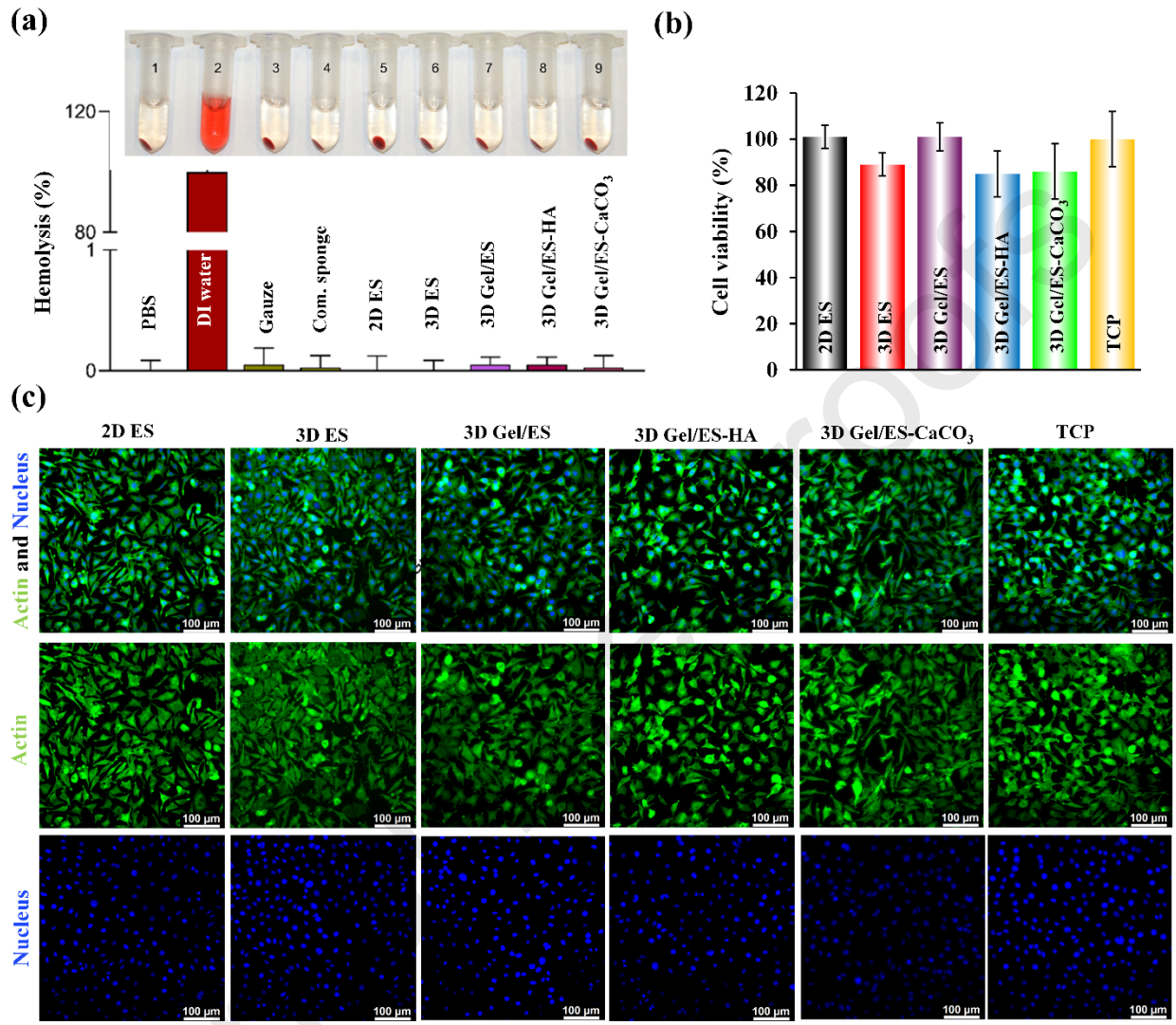

Figure 5. Hemocompatibility and cytocompatibility of the electrospun samples. Hemolysis ratio and photograph of RBCs treated with 2D fiber membrane and 3D fiber sponges (a). (1: PBS, 2: DI water, 3: Gauze, 4: Commercial sponge, 5: 2D ES, 6: 3D ES, 7: 3D Gel/ES, 8: 3D Gel/ES-HA, and 9: 3D Gel/ES-$CaCO_3$). Viability of L929 cells treated with 2D fiber membrane and 3D fiber sponges (b). Fluorescence microscopy images of L929 fibroblast morphology for 2D fiber membrane and 3D fiber sponges in comparison to TCP as a control: merged nucleus and actin (top), actin skeleton in green (middle), and cellular nucleus in blue (bottom) (c).

Ensuring the noncytotoxic nature of biomaterials is another critical requirement, as outlined in the International Organization for Standardization (ISO) 10993-1. It provides essential guidelines for the biological evaluation of medical devices. To assess cytotoxicity, L929 fibroblasts were exposed to extracts from 2D ES, 3D ES, 3D Gel/ES, 3D Gel/ES-HA, and 3D Gel/ES-$CaCO_3$, and their viability was evaluated using the Presto Blue assay after 24 h, with TCP serving as the control (Figure 5b). The results demonstrated that extracts from 2D ES and 3D Gel/ES exhibited higher cell viability compared to 3D ES and 3D Gel/ES with inorganic particles. All extract concentrations were classified as noncytotoxic, as cell viability exceeded 70% relative to TCP. Statistical analysis using two-way ANOVA with Tukey's multiple

comparisons revealed significant differences between 2D ES and both 3D Gel/ES and 3D Gel/ES-HA at full-strength (100%) extract concentrations ($p < 0.001$) (Fig. 5b). L929 fibroblasts, a type of adherent connective tissue cell responsible for extracellular matrix production, displayed similar morphology and distribution in contact with extracts from the tested samples compared to the control group after 24 h of incubation. Their shape and spreading behavior closely resembled that of cells cultured on TCP (Fig. 5c). The fibroblasts maintained well-defined intercellular interactions, extended filopodia and lamellipodia, and adhered effectively to the surface, indicating strong cell-material interaction.

3.4. *In vitro* hemostatic performance

To assess the hemostatic properties of the prepared samples, *in vitro* experiments on dynamic whole blood coagulation were performed. Medical gauze and a commercial sponge were chosen as control materials for effective comparison. According to Figure 6a, the leachates from the control samples and those from the 2D and 3D electrospun (ES) samples exhibited a red hue, indicating ineffective hemostasis. However, the leachates from the 3D Gel/ES-based sponges remained nearly transparent, signifying a superior capacity to coagulate blood. These results are consistent with the findings of the BCI (Figure 6b). The BCI was determined by measuring the absorbance value of the hemoglobin solution obtained from uncoagulated RBCs. In this assessment, a lower BCI value signifies a more rapid clotting rate, indicating superior hemostatic efficiency of the materials under investigation. The observed BCI for the various sample groups was as follows: 2D ES at 90.01 ± 1.5%, 3D ES at 74.01 ± 1.15%, 3D Gel/ES at 11.44 ± 0.69%, 3D Gel/ES-Ha at 13.35 ± 0.26%, and 3D Gel/ES-$CaCO_3$ at 10.18 ± 0.34%. These BCI values clearly demonstrate that the 3D Gel/ES-based sponge achieved a significantly faster clotting rate than the control (whole blood without any material; 100 ± 3.19%), gauze (92.46 ± 3.68%), and the commercial sponge (73.67 ± 3.96%). Moreover, the 2D and 3D ES samples also showed slower rates of clot formation and elevated BCI values, as they lacked the active hemostatic gelatin component. Therefore, the 2D ES and 3D ES samples were excluded from further evaluation in terms of coagulation function.

The coagulation performance of 3D Gel/ES-based sponges was additionally verified through an *in vitro* assay measuring blood clotting time, as illustrated in Figures 6c and d. The control group, consisting of whole blood without any material, exhibited a clotting time of 285 ± 36.97 s. All tested materials showed significantly shorter clotting times compared to the control. The coagulation time for the 3D Gel/ES fiber sponge was measured at 112.5 ± 17.07 s, comparable to gauze (110 ± 14.14 s) and quicker than a commercial sponge (155 ± 1.57 s). The reason for the shorter time could be that the 3D Gel/ES fiber sponge has a unique fluffy fiber structure, which dramatically increases surface area, and its superhydrophilic nature favors quick blood absorption to concentrate the blood cells.[40] Besides, the incorporation of different inorganic agents containing Ca^{2+} considerably improved the coagulation ability of 3D Gel/ES sponges, with clotting times of 60 ± 8.16 s for 3D Gel/ES-HA and 52 ± 9.57 s for 3D Gel/ES-$CaCO_3$ sponges, respectively. Thus, the obtained results demonstrate the efficiency of 3D Gel/ES hybrid fiber sponges. Essentially, promoting blood coagulation through their 3D physical structure, rapid blood water absorption, accumulation, and concentration of RBCs and platelets, as well as the faster activation of coagulation factors. A key characteristic contributing to this enhanced coagulation capability is the synergistic effect of the functional carboxylate groups present on the sponge surfaces and the inorganic agents incorporated into the 3D matrix. The high negative surface potential created by deprotonated carboxylate groups absorbs blood components such as fibrinogen and coagulation factors.[62] Simultaneously, the incorporated inorganic agents help to establish an elevated concentration of Ca^{2+}, which is critical in various coagulation pathways.[9,64]

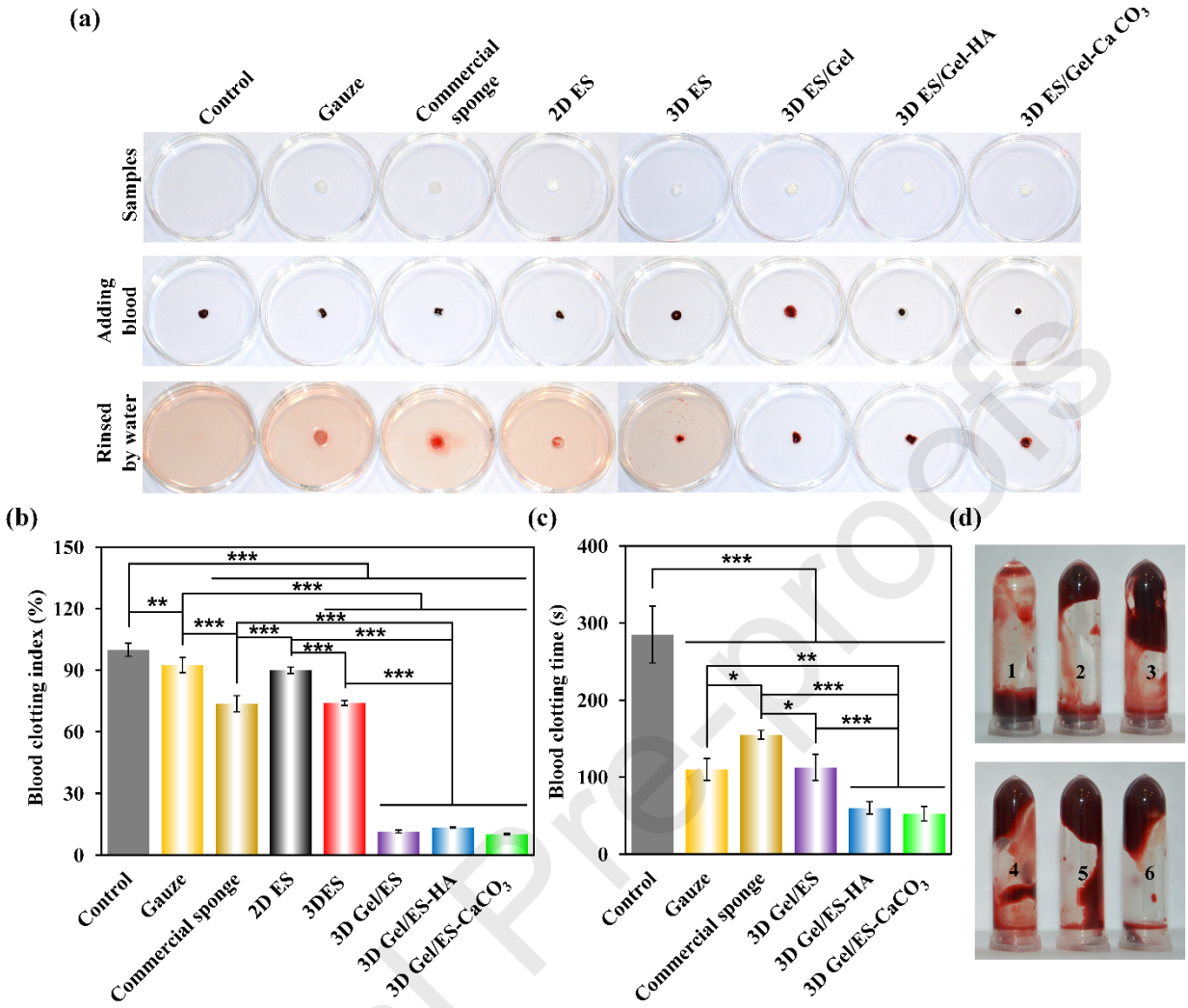

Figure 6. *In vitro* hemostatic performance of different electrospun samples. Photographs of a dynamic whole-blood coagulation process (a) and the corresponding BCI values of samples (b). *In vitro* whole-blood clotting time of samples (c), and photographs of blood clotting time measurement (1: Control, 2: Gauze, 3: Commercial sponge, 4: 3D Gel/ES fiber sponge, 5: 3D Gel/ES-HA fiber sponge, and 6: 3D Gel/ES-$CaCO_3$ fiber sponge).

3.5. RBC and platelet adhesion performances of the 3D Gel/ES-based fiber sponges

An essential step of physiological hemostasis is the aggregation and activation of blood components, which work together to form blood clots that serve as effective physical barriers. The adherence and stable aggregation of RBCs, which are vital for thrombus formation, play a significant role in initiating and maintaining the coagulation process.[65] Additionally, platelets are essential contributors to hemostasis and thrombosis, with their strong adhesion leading to both platelet aggregation and activation.[66] Therefore, we closely examined the surface adhesion and morphologies of erythrocytes and platelets on the 3D Gel/ES-based fiber sponges, comparing them to the control materials. Figure 7 illustrates both the qualitative and quantitative outcomes of these examinations. As shown in Figure 7a, all tested materials showed markedly lower erythrocyte adhesion compared to the control (100 ± 3.21%), which consisted of a mixture of RBC suspension and DI water without exposure to any test material. Among the

reference materials, gauze and commercial sponges showed a low adhesion rate of erythrocytes, with only 9.07 ± 0.32% and 9.66 ±0.54% adhesion, respectively. The 3D Gel/ES fiber sponge displayed a higher erythrocyte adhesion rate of 33.35 ± 2.41% compared to the control groups, indicating that the 3D Gel/ES sponge promoted adhesion. The improvement in capturing erythrocytes cannot be attributed solely to the increased blood contact area in the fabricated sponge's fluffy, interconnected porous structure.[40] It is also due to its high porosity, abundant negatively charged functional groups, deprotonated carboxylate-induced superhydrophilicity, and impressive blood absorbency, which contribute to its enhanced adhesion performance. Furthermore, a hybrid sponge with the inclusion of HA that has identical fiber structures with 3D Gel/ES exhibited an increased RBC adhesion rate (58.22 ± 10.52%), suggesting that HA nanoparticles greatly promote RBC adhesion by releasing Ca^{2+} ions. A noteworthy observation is that a 3D Gel/ES-$CaCO_3$ sponge incorporating another calcium-containing compound exhibited a remarkably high RBC adhesion ratio (83.96 ± 6.03%), significantly surpassing that of the 3D Gel/ES-HA. The enhanced adhesive properties can likely be attributed to the generation of a high-concentration calcium microenvironment, facilitated by a distinct release rate of Ca^{2+} ions from the $CaCO_3$ compound. Despite both the $CaCO_3$ and HA particles containing a similar mass percentage of approximately 40% calcium,[67] the different ionic release dynamics appear to significantly influence the overall RBC adhesion capabilities of the hybrid sponges. The adhesion behavior of RBCs to the 3D Gel/ES and its hybrid fiber sponges was also corroborated through SEM analysis (Figure 7d). The morphological analysis revealed the varying presence and distribution of adhered RBCs on fabricated sponges and control samples. Additionally, they confirmed the formation of a densely packed array of polyhedral erythrocytes, known as polyhedrocytes, which may play a crucial role in creating an impermeable barrier that can effectively stop bleeding.[19,68] In detail, limited numbers of erythrocytes adhered to the gauze and commercial sponge, while significantly greater numbers of RBCs were absorbed by the 3D electrospun sponges and trapped in the inner part of the loosely packed fibers of those sponges due to their fluffy and porous design. Moreover, a notable transformation in the shape of erythrocytes was observed; they exhibited a shift from their characteristic biconcave form to polyhedral shapes when interacting with the 3D fiber sponges. The transformation within the 3D Gel/ES-$CaCO_3$ sponge exhibited most polyhedral erythrocytes and tightly aggregated, forming larger polygonal cell clusters. This behavior is intricately linked to erythrocyte activation and the contraction processes associated with blood clot formation.[69]

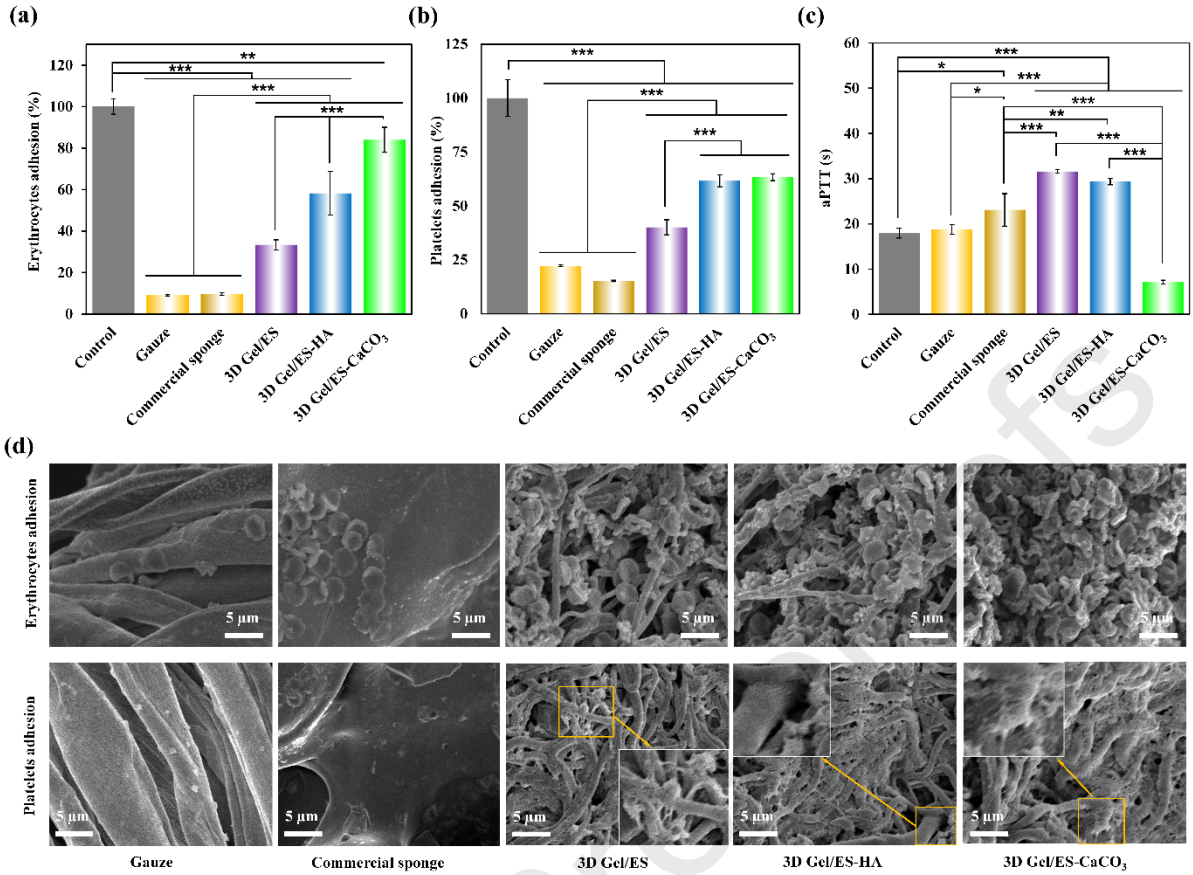

Figure 7. The hemostatic mechanism of the 3D Gel/ES-based fiber sponges. The percentage of adhered erythrocytes (a) and platelets (b) on the surface of gauze, commercial sponge, 3D Gel/ES, 3D Gel/ES-HA, and 3D Gel/ES-$CaCO_3$ fibers. aPTT values of each sample group (c). Representative SEM micrographs of RBC and platelet adhesion on the surface of gauze, commercial sponge, 3D Gel/ES, 3D Gel/ES-HA, and 3D Gel/ES-$CaCO_3$ fibers (d).

Regarding platelet adhesion, the fabricated sponges and control materials were incubated for 30 min with PRP. To assess platelet counts, we employed the LDH assay. Higher levels of LDH indicate a greater degree of platelet adsorption onto the materials, which is illustrated in Figure 7b. The adhesion of platelets to gauze, commercial sponge, and 3D Gel/ES fiber sponge exhibited a trend similar to the erythrocyte adhesion results observed with those samples. All tested materials showed lower platelet adhesion compared to the control (100 ± 8.49), which consisted of PRP without any material. The gauze and commercial sponge demonstrated low platelet adhesion (22.21 ± 0.42% and 15.23 ± 0.36%), while the 3D Gel/ES fiber sponge showed a slightly enhanced interaction (40.06 ± 3.49 %), possibly due to its previously mentioned unique structural characteristics and surface chemistry. In the context of 3D Gel/ES hybrid fiber sponges, the presence of HA and $CaCO_3$ has been shown to significantly improve platelet adhesion, as each of these inorganic additives effectively contributes to the activation of the coagulation cascade.[64] Principally, there was no significant difference in platelet adhesion between the fiber sponges containing HA (61.63 ± 2.73%) and those containing $CaCO_3$ (63.33 ± 1.61%). In addition, the crucial function of platelets in coagulation involves three phases: adhesion, activation, and aggregation. Therefore, SEM analysis is particularly valuable for observing platelet activation and aggregation on the fibers of sponges. In general, platelet activation is directly linked to the size of the area containing platelets and the formation of pseudopodia. In Figure 7d, it is observed that small individual platelets with spherical areas and no pseudopodia were dispersed on the gauze and commercial sponge, indicating an inactivated

platelet state. Although the pseudopodia of the platelets were observed to be extended partially on 3D Gel/ES fibers, thereby facilitating the attachment of a larger number of platelets to the sponge, there was still the presence of inactivated platelets. The new emerging direct and non-direct impact factors for changing platelets' physiological states within the 3D Gel/ES fiber sponge were its carboxylate-functionalization and a stable 3D nanofiber architecture possessing interconnected pores without compromising the functionality of the intrinsic nanofibers. In contrast, abundant platelet aggregates and substantial platelets with more extended and surrounded pseudopodia formations were observed within both 3D Gel/ES fiber sponges containing calcium compounds, a representative feature of activated platelets compared with other sample groups. It can be inferred that 3D hybrid fiber sponges releasing Ca^{2+} may result in a rise in free Ca^{2+}, which enhances the expression of glycoprotein IIb/IIIa (a platelet surface receptor) and the binding of fibrinogen to platelets, and would synergistically accelerate platelet activation.[27] In parallel, the elevated negative charges of those sponges are advantageous for triggering the activation of clotting factors and the coagulation cascade, while the hydrophilic carboxylate groups are likely to damage platelets.[15,70] Moreover, the micrographs revealed that activated platelets, which aid in the conversion of soluble fibrinogen into insoluble fibrin monomer, began to build a "spider web-like fibrin network" of aggregation through the entanglement of pseudopodia, which was a vital sign of procoagulant.[15,19,20]

The effects of the 3D Gel/ES-based fiber sponges on the extrinsic and intrinsic coagulation pathways were evaluated by measuring the PT and aPTT, respectively. As shown in Figure 7c, 3D Gel/ES and 3D Gel/ES-HA fiber sponges showed a slight increase in aPPT values compared with the control group (plasma without any added material), while all remained within the normal range. There were no statistically significant differences in PT levels between all experimental groups and control groups (Figure S2, Supporting Information). These results indicated that the studied samples did not adsorb coagulation factors in PPP or had a minimal impact on the initiation of traditional intrinsic and extrinsic coagulation pathways and did not affect human coagulation factor activity. It is widely known that the intricate process of blood clotting is fundamentally reliant on the dynamic interplay of various components, primarily the activity of plasma coagulation factors, as well as the quantity and quality of functional platelets and erythrocytes.[71] Since there were no clear enhancements in the activation of plasma coagulation factors by 3D Gel/ES-HA, we assume that the procoagulation was a result of 3D Gel/ES-HA's effects on erythrocytes and/or platelets, as well as an external coagulation cascade that accelerates fibrin synthesis.[19,71] Interestingly, the clotting time of PPP treated with a 3D Gel/ES hybrid sponge containing $CaCO_3$ compound was significantly shortened (by 60%) compared to the control, indicating that 3D Gel/ES-$CaCO_3$ could enhance the intrinsic coagulation pathway. Overall, activating the intrinsic pathway of the coagulation cascade, along with the adhesion, enrichment, and activation properties of erythrocytes and platelets, led to the best hemostatic performance in the 3D Gel/ES hybrid fiber sponges *in vitro*, particularly in the 3D Gel/ES-$CaCO_3$. This dynamic interaction illustrates the potential of these sponges as effective hemostatic agents *in vivo*.

3.6. *In vivo* hemostatic performance

The 3D Gel/ES hybrid fiber sponges demonstrated the shortest time for blood clotting in an *in vitro* assay, prompting further assessment of their hemostatic effectiveness in both the rat liver hemorrhage and tail amputation models (Figure 8a-c). As shown in Figures 8d and e, an *in vivo* hemostasis evaluation was conducted using a rat liver injury model. There were no statistically significant differences in the body weight of rats among the experimental groups during the

study. The mean body weights were 192.0 ± 7.7 g for the gauze group, 189.6 ± 5.4 g for the commercial sponge group, 187.8 ± 6.5 g for the 3D Gel/ES-HA group, and 194.0 ± 3.5 g for the 3D Gel/ES-$CaCO_3$ group. The *in vivo* hemostatic assessment of the 3D Gel/ES hybrid sponge samples demonstrated a strong correlation with the previously established *in vitro* hemostatic performance. In detail, the mean bleeding time for the gauze group was 153 ± 24 s, while the average blood loss was 138.74 ± 11.92 mg. The commercial gelatin sponge reduced clotting time by 10% and bleeding volume by 31%. Rats treated with the 3D Gel/ES-HA and 3D Gel/ES-$CaCO_3$ fiber sponges exhibited significantly shorter bleeding times of 43 ± 6.78 and 44 ± 7.7 s, respectively, with blood losses of 31.53 ± 17.64 and 26.37 ± 9.99 mg. These results corresponded to reductions in clotting time of 72% and 71% and decreases in blood volume of 77% and 81% compared to the control gauze group.

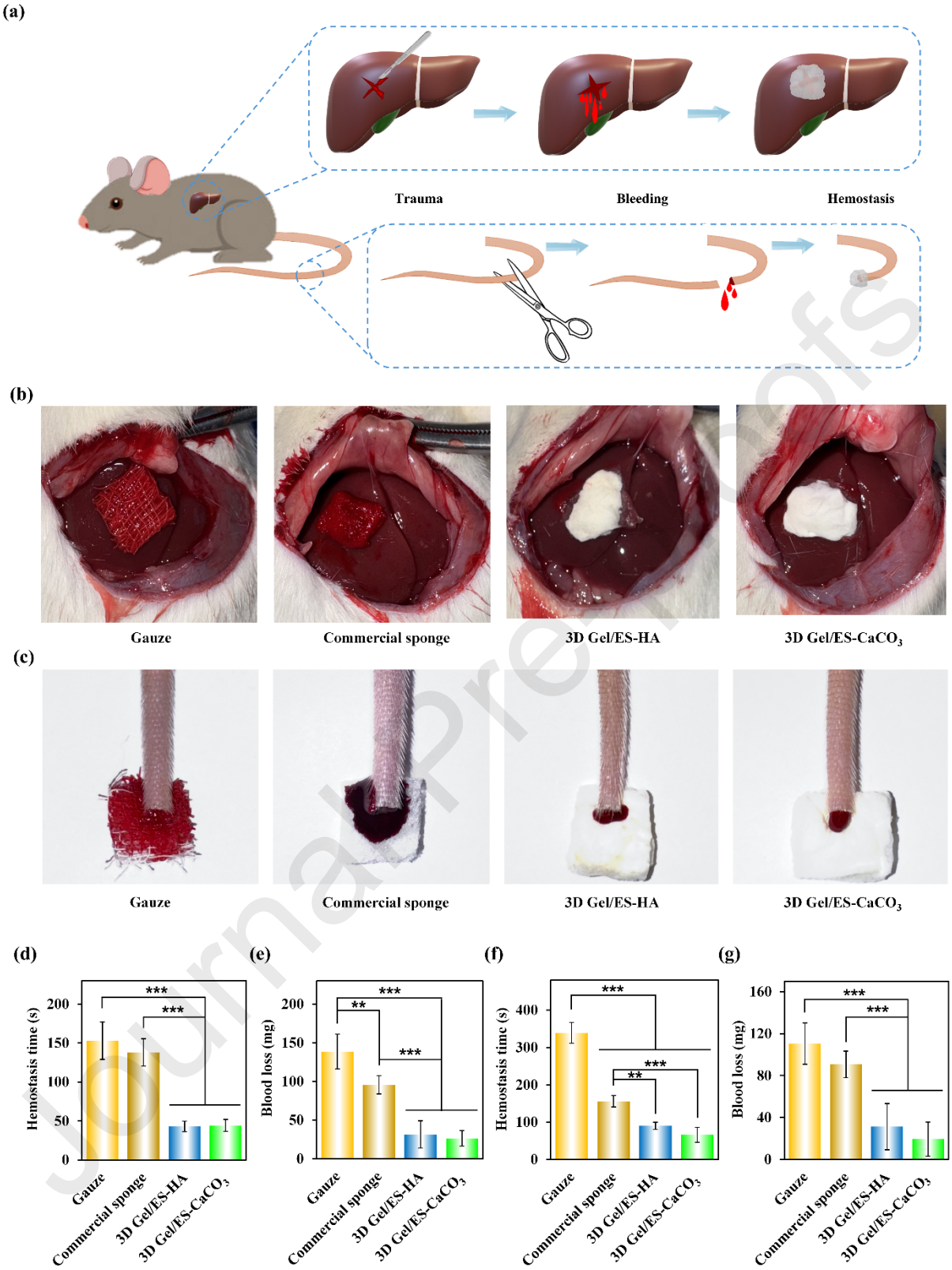

Figure 8. *In vivo* hemostatic performance of the 3D Gel/ES hybrid sponges. Schematic diagram of hemostatic procedure for bleeding of the rat liver injury and tail amputation model (a). Photographs of the hemostatic effect of samples on the liver injury (b) and tail amputation (c). Hemostasis time and blood loss from bleeding of rat livers (d and e). Hemostasis time and blood loss from bleeding of rat tails (f and g).

An additional *in vivo* study was performed using a rat tail amputation model (Figure 8f and g). Similarly to the liver injury model, no significant differences in body weight were observed among groups in the liver injury model. The mean body weights were 187.0 ± 4.4 g for the gauze group, 190.6 ± 6.3 g for the commercial sponge group, 193.0 ± 5.9 g for the 3D Gel/ES-HA group, and 188.2 ± 3.8 g for the 3D Gel/ES-$CaCO_3$ group. The gauze control group exhibited an average bleeding time of 339 ± 27.82 s and an average blood loss of 110 ± 19.73 mg. The application of various hemostatic dressings significantly decreased both bleeding time and total blood loss. The 3D Gel/ES-HA sponge substantially shortened the bleeding time to an average of 90 ± 9.48 s while reducing blood loss to 31.32 ± 22.12 mg. The 3D Gel/ES-$CaCO_3$ fiber sponge further reduced the average hemostasis time to 66 ± 20.43 s, with blood loss decreasing to 19.43 ± 16.32 mg. Furthermore, the 3D Gel/ES hybrid sponges outperformed the commercial gelatin sponge, which had an average hemostasis time of 156 ± 15.29 s and a blood loss of 90.72 ± 17.7 mg. The collective findings from the in vivo study provide robust evidence that the 3D Gel/ES-$CaCO_3$ fiber sponge effectively promotes hemostasis in mild-to-moderate bleeding models. Compared with recent studies on gelatin-based hemostatic sponges (Table S1, Supporting Information), Gel/ES hybrid fiber sponges prepared by a simple, one-step method have a considerable advantage in reducing hemostatic time and blood loss, thereby reinforcing the present study's innovation and practical value. Further studies, including femoral artery injury models, are warranted to evaluate its potential for managing severe and non-compressible hemorrhages.

Based on comprehensive *in vitro* and *in vivo* evaluations of hemostatic performance, we hypothesized a synergistic hemostatic mechanism for the 3D Gel/ES hybrid fiber sponge, including physical interactions and enhanced coagulation stimulants. (Figure 9). When the superhydrophilic 3D sponge is applied to the bleeding site, its light and highly porous structure facilitates the rapid extraction of fluid from the blood. Simultaneously, continuous and interconnected fibers effectively promoted the aggregation of platelets and RBCs, allowing for the development of a preliminary bundle of sponge and blood cells. During this process, deprotonated carboxyl groups, as well as the Ca^{2+} released from the hybrid fibers, triggered coagulation factors via the intrinsic pathway, affecting their activating role on platelets and RBCs. 3D Gel/ES-$CaCO_3$ fiber enabled plentiful RBCs to adhere and aggregate into polyhedrocytes. It facilitated substantial platelets exhibiting elongated and intricately structured pseudopodia, effectively synergizing to speed up platelet activation, forming tightly packed cell clusters. Ultimately, such a tight cluster of fiber sponge-platelets-polyhedrocytes may merge with an insoluble fibrin fiber network to form a thrombus, establishing a strongly stable hemostatic barrier in the short term.

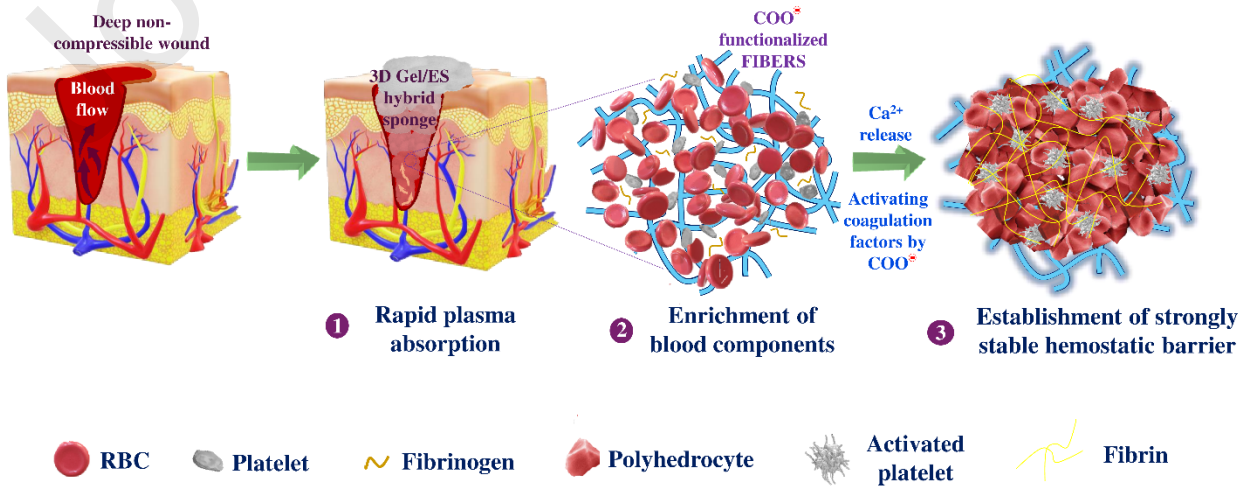

Figure 9. Schematic illustration of the hemostatic mechanisms of the 3D Gel/ES hybrid fiber sponge.

An extensive evaluation of the overall efficacy of deprotonated carboxylate-functionalized 3D hybrid fiber sponges as biodegradable implantable hemostatic agents tailored for managing visceral organ hemorrhages has been planned. This will include *in vivo* studies over a prolonged period to better understand their performance, longevity, and integration within biological systems. The long-term follow-up study aims to provide critical insights into the safety, biocompatibility, and potential clinical applications of these innovative hemostatic materials in surgical and trauma settings.

4. Conclusion

In this study, we present a successful development of a novel one-step electrospinning strategy for the fabrication of carboxylate-functionalized 3D Gel/ES-based sponges designed for rapid hemostasis. Particularly addressing the challenges in the development of hybrid multifunctional materials for effective hemorrhage control. Facilitated by the deprotonation of carboxyl groups in ES, electrospinning led to the generation of fluffy, highly porous, and interconnected fiber morphology. The fiber sponges obtained by exploiting electrostatic repulsion among fiber surfaces during electrospinning resulted in a substantial, interconnected porous architecture, superhydrophilicity, good elasticity, and a negative surface potential. Physicochemical analyses of generated fibers support their suitability as mechanically stable and physiologically effective hemostatic materials. Furthermore, functionalization of fibers using inorganic bioactive agents such as hydroxyapatite and $CaCO_3$ improved their hemostatic effectiveness. Functionally, the formation of a stable blood clot within the 3D Gel/ES hybrid sponges is promoted by contributing to the activation of platelets and the enrichment of erythrocytes into a polyhedron. *In vivo* studies further confirmed their multifunctionality in hemostasis, which is synergistically powered by a rapid release rate of Ca^{2+} ions and an abundance of deprotonated carboxylate groups. As highlighted via rat tail amputation and liver injury model study, 3D Gel/ES-HA and 3D Gel/ES-$CaCO_3$ exerted a robust sealing effect on the bleeding site, with a short hemostasis time and less blood loss compared to commercial agents. The proposed strategy offers an effective, multifunctional platform for practical hemorrhage control in mild-to-moderate bleeding scenarios. The resulting 3D nanofiber sponges are well-suited for further optimization toward industrial scalability, presenting a clinically and commercially viable solution with strong translational potential. Future work will focus on evaluating their efficacy in additional bleeding models, as well as their safety, biocompatibility, and clinical applicability.

Acknowledgements

Author AA sincerely acknowledges the financial support from the Alexander von Humboldt Foundation (Experienced Researcher Fellowship, grant agreement ID: MNG 1237848 HFST-E). BK acknowledges the financial support from the Medical University of Bialystok, Poland. Authors RH would like to thank Prof. Dr. Björn Neu and Timo Preißing for access to the Zetasizer, and Prof. Dr. Kerstin Koch and Axel Huth for access to the Goniometer, both at the Faculty of Life Sciences at the Rhine-Waal University of Applied Sciences, Kleve.

Conflict of Interest

The authors declare no conflict of interest.

Data availability

Data will be made available on request.

References

[1] P. Bouzat, G. Valdenaire, T. Gauss, J. Charbit, C. Arvieux, P. Balandraud, X. Bobbia, J.S. David, J. Frandon, D. Garrigue, J.A. Long, J. Pottecher, B. Prunet, B. Simonnet, K. Tazarourte, C. Trésallet, J. Vaux, D. Viglino, B. Villoing, L. Zieleskiewicz, C. Gil-Jardiné, E. Weiss, Early management of severe abdominal trauma, Anaesth Crit Care Pain Med 39 (2020) 269–277. https://doi.org/10.1016/J.ACCPM.2019.12.001.

[2] J.F. Kragh, T.J. Walters, D.G. Baer, C.J. Fox, C.E. Wade, J. Salinas, J.B. Holcomb, Survival with emergency tourniquet use to stop bleeding in major limb trauma, Ann Surg 249 (2009) 1–7. https://doi.org/10.1097/SLA.0B013E31818842BA.

[3] K. Kim, J.H. Ryu, M.Y. Koh, S.P. Yun, S. Kim, J.P. Park, C.W. Jung, M.S. Lee, H. Il Seo, J.H. Kim, H. Lee, Coagulopathy-independent, bioinspired hemostatic materials: A full research story from preclinical models to a human clinical trial, Sci Adv 7 (2021) 9992–10016. https://doi.org/10.1126/SCIADV.ABC9992/SUPPL_FILE/ABC9992_SM.PDF.

[4] S. Pourshahrestani, E. Zeimaran, N.A. Kadri, N. Mutlu, A.R. Boccaccini, Polymeric Hydrogel Systems as Emerging Biomaterial Platforms to Enable Hemostasis and Wound Healing, Adv Healthc Mater 9 (2020) 2000905. https://doi.org/10.1002/ADHM.202000905.

[5] Y. Zheng, J. Wu, Y. Zhu, C. Wu, Inorganic-based biomaterials for rapid hemostasis and wound healing, Chem Sci 14 (2022) 29–53. https://doi.org/10.1039/D2SC04962G.

[6] M. Mecwan, J. Li, N. Falcone, M. Ermis, E. Torres, R. Morales, A. Hassani, R. Haghniaz, K. Mandal, S. Sharma, S. Maity, F. Zehtabi, B. Zamanian, R. Herculano, M. Akbari, J. V. John, A. Khademhosseini, Recent advances in biopolymer-based hemostatic materials, Regen Biomater 9 (2022). https://doi.org/10.1093/RB/RBAC063.

[7] J. Park, T.Y. Kim, Y. Kim, S. An, K.S. Kim, M. Kang, S.A. Kim, J. Kim, J. Lee, S.W. Cho, J. Seo, A Mechanically Resilient and Tissue-Conformable Hydrogel with Hemostatic and Antibacterial Capabilities for Wound Care, Advanced Science 10 (2023) 2303651. https://doi.org/10.1002/ADVS.202303651;PAGE:STRING:ARTICLE/CHAPTER.

[8] W. Fang, L. Yang, Y. Chen, Q. Hu, Bioinspired multifunctional injectable hydrogel for hemostasis and infected wound management, Acta Biomater 161 (2023) 50–66. https://doi.org/10.1016/J.ACTBIO.2023.01.021.

[9] G. He, Z. Chen, L. Chen, H. Lin, C. Yu, T. Zhao, Z. Luo, Y. Zhou, S. Chen, T. Yang, G. He, W. Sui, Y. Hong, J. Zhao, Hydroxyapatite/calcium alginate composite particles for hemostasis and alveolar bone regeneration in tooth extraction wounds, PeerJ 11 (2023) e15606. https://doi.org/10.7717/PEERJ.15606/SUPP-25.

[10] C. Zheng, J. Liu, Q. Bai, Y. Quan, Z. Li, W. Chen, Q. Gao, Y. Zhang, T. Lu, Preparation and hemostatic mechanism of bioactive glass-based membrane-like structure camouflage composite particles, Mater Des 223 (2022) 111116. https://doi.org/10.1016/J.MATDES.2022.111116.

[11] M. Stark, A.Y. Wang, B. Corrigan, H.G. Woldu, S. Azizighannad, G. Cipolla, R. Kocharian, H. De Leon, Comparative analyses of the hemostatic efficacy and surgical device performance of powdered oxidized regenerated cellulose and starch-based powder formulations, Res Pract Thromb Haemost 9 (2025) 102668. https://doi.org/10.1016/J.RPTH.2024.102668.

[12] K. Yao, S. Li, X. Zheng, Q. Zhang, J. Liu, C. Liang, K. Duan, J. Ye, Y. Yin, X. Chen, Superwettable calcium ion exchanged carboxymethyl cellulose powder with self-gelation, tissue adhesion and bioabsorption for effective hemorrhage control, Chemical Engineering Journal 481 (2024) 148770. https://doi.org/10.1016/J.CEJ.2024.148770.

[13] F. Cheng, X. Yi, J. Dai, Z. Fan, J. He, Y. Huang, H. Li, Photothermal MXene@Zn-MOF-decorated bacterial cellulose-based hydrogel wound dressing for infectious wound healing, Cell Rep Phys Sci 4 (2023) 101619. https://doi.org/10.1016/J.XCRP.2023.101619.

[14] L. Yuan, X. Jiang, M. Jiang, Y. Guo, Y. Liu, P. Ming, S. Li, P. Zhou, R. Cai, K. Yu, G. Tao, Biocompatible gellan gum/sericin hydrogels containing halloysite@polydopamine nanotubes with hemostasis and photothermal antibacterial properties for promoting infectious wound repair, Mater Des 227 (2023) 111744. https://doi.org/10.1016/J.MATDES.2023.111744.

[15] Y. Lv, Y. Xu, S. Zhang, S. Xie, B. Wang, T. Sun, X. Zhang, S. Yao, H. Zhang, L. Wang, L.N. Wang, Rapidly Photocurable and Strongly Adhesive Hydrogel-Based Sealant with Good Procoagulant Activity for Lethal Hemorrhage Control, Adv Funct Mater (2025) 2501904. https://doi.org/10.1002/ADFM.202501904;JOURNAL:JOURNAL:10990712;PAGE:STRING:ARTICLE/CHAPTER.

[16] M. Ghovvati, S. Jain, G.Z. Cheng, N. Kaneko, J.A. Boys, T. Imahori, T. De Maeseneer, R. Haghniaz, R.B. Cameron, A.S. Weiss, N. Annabi, Rapid closure and hemostasis of ruptured soft tissues using a modified human tropoelastin-based sealant in preclinical models, Sci Transl Med 17 (2025) eadr6458. https://doi.org/10.1126/SCITRANSLMED.ADR6458/SUPPL_FILE/SCITRANSLMED.ADR6458_MDAR_REPRODUCIBILITY_CHECKLIST.PDF.

[17] P. Cai, L. Cao, Y. Ding, Y. Han, X. Yu, J. Cui, H. Wang, J. Wu, M. EL-Newehy, M.M. Abdulhameed, X. Mo, S. Wang, B. Sun, Modified Highly Elastic 3D Nanofiber Embolic Scaffolds for Precise In Situ Embolization Therapy, Adv Funct Mater 34 (2024) 2316590. https://doi.org/10.1002/ADFM.202316590;REQUESTEDJOURNAL:JOURNAL:16163028;WGROUP:STRING:PUBLICATION.

[18] X. Lu, X. Li, J. Yu, B. Ding, Nanofibrous hemostatic materials: Structural design, fabrication methods, and hemostatic mechanisms, Acta Biomater 154 (2022) 49–62. https://doi.org/10.1016/J.ACTBIO.2022.10.028.

[19] J. Zhang, Z. Chen, D. Zeng, Y. Xia, Y. Fan, X. Zhang, N. Li, X. Liu, X. Sun, S. Zhao, J. Zhang, J. Liu, Q. Sun, Antibacterial and rapidly absorbable hemostatic sponge by aldehyde modification of natural polysaccharide, Communications Materials 2024 5:1 5 (2024) 1–21. https://doi.org/10.1038/s43246-024-00579-0.

[20] S. Salmanipour, A. Rezaie, N. Alipour, M. Ghahremani-Nasab, M.S. Zakerhamidi, N. Akbari-Gharalari, A. Mehdipour, R. Salehi, S. Jarolmasjed, Development of Polyphosphate/Nanokaolin-Modified Alginate Sponge by Gas-Foaming and Plasma Glow Discharge Methods for Ultrarapid Hemostasis in Noncompressible Bleeding, ACS Applied Materials and Interfaces 16 (2024) 34684–34704. https://doi.org/10.1021/ACSAMI.4C05695/SUPPL_FILE/AM4C05695_SI_013.MP4.

[21] Y. Liang, C. Xu, F. Liu, S. Du, G. Li, X. Wang, Eliminating Heat Injury of Zeolite in Hemostasis via Thermal Conductivity of Graphene Sponge, ACS Appl Mater Interfaces 11 (2019) 23848–23857. https://doi.org/10.1021/ACSAMI.9B04956/SUPPL_FILE/AM9B04956_SI_001.PDF.

[22] H.T. Beaman, E. Shepherd, J. Satalin, S. Blair, H. Ramcharran, S. Serinelli, L. Gitto, K.S. Dong, D. Fikhman, G. Nieman, S.G. Schauer, M.B.B. Monroe, Hemostatic shape memory polymer foams with improved survival in a lethal traumatic hemorrhage model, Acta Biomater 137 (2022) 112–123. https://doi.org/10.1016/J.ACTBIO.2021.10.005.

[23] X. Jia, Y. Luo, F. Yang, X. Wu, L. Diao, O.W. Ojo, Y. Zhang, X. Liu, H. Liang, W. Zhong, K. Mequanint, M. Xing, G. Lyu, Hierarchically oriented foam with thermal management performance for hemorrhage control and wound healing, Chemical Engineering Journal 509 (2025) 161052. https://doi.org/10.1016/J.CEJ.2025.161052.

[24] M.T. Perelló-Trias, A. Rodríguez-Fernández, A.J. Serrano-Muñoz, J.J. Segura-Sampedro, P. Tauler, J.M. Ramis, M. Monjo, Evaluation of Different Commercial Sealing Hemostatic Patches for Their Selection as Reservoirs for Localized Intraperitoneal Chemotherapy, ACS Pharmacol Transl Sci 8 (2025) 499–509. https://doi.org/10.1021/ACSPTSCI.4C00608.

[25] O. Shaeer, A. Elahwany, H. El Debs, A. Ragheb, K.O.K.M. Shaeer, K. Shaeer, Application of gelatin sponge (Gelfoam®) as a hemostatic agent in inflatable

penile prosthesis implantation, International Journal of Impotence Research 2025 (2025) 1–4. https://doi.org/10.1038/s41443-025-01184-6.

[26] Y. Yang, Y. Du, J. Zhang, H. Zhang, B. Guo, Structural and Functional Design of Electrospun Nanofibers for Hemostasis and Wound Healing, Advanced Fiber Materials 2022 4:5 4 (2022) 1027–1057. https://doi.org/10.1007/S42765-022-00178-Z.

[27] L. Tan, X. Zhou, K. Wu, D. Yang, Y. Jiao, C. Zhou, Tannic acid/CaII anchored on the surface of chitin nanofiber sponge by layer-by-layer deposition: Integrating effective antibacterial and hemostatic performance, Int J Biol Macromol 159 (2020) 304–315. https://doi.org/10.1016/J.IJBIOMAC.2020.05.098.

[28] A. Amarjargal, O. Cegielska, D. Kolbuk, B. Kalaska, P. Sajkiewicz, On-Demand Sequential Release of Dual Drug from pH-Responsive Electrospun Janus Nanofiber Membranes toward Wound Healing and Infection Control, ACS Appl Mater Interfaces 16 (2024) 153–165. https://doi.org/10.1021/ACSAMI.3C13676/ASSET/IMAGES/MEDIUM/AM3C13676_0008.GIF.

[29] X. Yu, Z. Gao, J. Mu, H. Lian, Z. Meng, Gelatin/calcium chloride electrospun nanofibers for rapid hemostasis, Biomater Sci 11 (2023) 2158–2166. https://doi.org/10.1039/D2BM01767A.

[30] H. Chen, J. Yan, S. Hu, S. Sun, F. Zhou, J. Liu, S. Tang, Q. Zhou, H. Ding, F. Zhang, N. Gu, Janus fibre/sponge composite combined with IOPNs promotes haemostasis and efficient reconstruction in oral guided bone regeneration, Mater Des 222 (2022) 111083. https://doi.org/10.1016/J.MATDES.2022.111083.

[31] V.P. Nirwan, A. Amarjargal, R. Hengsbach, A. Fahmi, Electrospun Smart Hybrid Nanofibers for Multifaceted Applications, Macromol Rapid Commun (2024) 2400617. https://doi.org/10.1002/MARC.202400617;REQUESTEDJOURNAL:JOURNAL:15213927;PAGE:STRING:ARTICLE/CHAPTER.

[32] A. Amarjargal, Z. Moazzami Goudarzi, O. Cegielska, A. Gradys, D. Kolbuk, B. Kalaska, A. Ruszczyńska, P. Sajkiewicz, A facile one-stone-two-birds strategy for fabricating multifunctional 3D nanofibrous scaffolds, Biomater Sci 11 (2023) 5502–5516. https://doi.org/10.1039/D3BM00837A.

[33] T. Liu, S. Liu, Y. Shi, Z. Zhang, S. Ding, K. Hou, W. Zhang, X. Meng, F. Li, Electrospun nanofiber membranes for rapid liver hemostasis via N-alkylated chitosan doped chitosan/PEO, Int J Biol Macromol 258 (2024) 128948. https://doi.org/10.1016/J.IJBIOMAC.2023.128948.

[34] P. Sasmal, P. Datta, Tranexamic acid-loaded chitosan electrospun nanofibers as drug delivery system for hemorrhage control applications, J Drug Deliv Sci Technol 52 (2019) 559–567. https://doi.org/10.1016/J.JDDST.2019.05.018.

[35] H. Chen, J. Yan, S. Hu, S. Sun, F. Zhou, J. Liu, S. Tang, Q. Zhou, H. Ding, F. Zhang, N. Gu, Janus fibre/sponge composite combined with IOPNs promotes haemostasis and efficient reconstruction in oral guided bone regeneration, Mater Des 222 (2022) 111083. https://doi.org/10.1016/J.MATDES.2022.111083.

[36] R. Dong, H. Zhang, B. Guo, Emerging hemostatic materials for non-compressible hemorrhage control, Natl Sci Rev 9 (2022). https://doi.org/10.1093/NSR/NWAC162.

[37] L. Yao, H. Gao, Z. Lin, Q. Dai, S. Zhu, S. Li, C. Liu, Q. Feng, Q. Li, G. Wang, X. Chen, X. Cao, A shape memory and antibacterial cryogel with rapid hemostasis for noncompressible hemorrhage and wound healing, Chemical Engineering Journal 428 (2022) 131005. https://doi.org/10.1016/J.CEJ.2021.131005.

[38] K. Fang, C. Wang, Y. Yang, F. Tang, F. Huang, Ultralight 3D silk nanofiber scaffolds with enhanced hemostatic properties and biocompatibility for rapid hemostasis, Mater Today Commun 41 (2024) 110592. https://doi.org/10.1016/J.MTCOMM.2024.110592.

[39] K. Zhang, X. Bai, Z. Yuan, X. Cao, X. Jiao, Y. Li, Y. Qin, Y. Wen, X. Zhang, Layered nanofiber sponge with an improved capacity for promoting blood coagulation and wound healing, Biomaterials 204 (2019) 70–79. https://doi.org/10.1016/J.BIOMATERIALS.2019.03.008.

[40] X. Xie, D. Li, Y. Chen, Y. Shen, F. Yu, W. Wang, Z. Yuan, Y. Morsi, J. Wu, X. Mo, Conjugate Electrospun 3D Gelatin Nanofiber Sponge for Rapid Hemostasis, Adv Healthc Mater 10 (2021) 2100918. https://doi.org/10.1002/ADHM.202100918.

[41] S.Y. Hu, J.C. Lv, M. Yan, J.Y. Wu, Z.G. Wang, R. Hong, J.X. Gou, L. Li, K. Li, J.Z. Xu, Z.M. Li, Multifunctional Electrospun Fiber Sponge for Hemostasis and Infected Wound Healing, Small 21 (2025) 2409969. https://doi.org/10.1002/SMLL.202409969;CTYPE:STRING:JOURNAL.

[42] A. Amarjargal, O. Miler, V.P. Nirwan, R. Hengsbach, P. Sajkiewicz, A. Fahmi, Facile Fabrication of Antibacterial 3D Fibrous Sponge via In Situ Protonation-Induced Direct Electrospinning, Adv Mater Interfaces 12 (2025) 2400935. https://doi.org/10.1002/ADMI.202400935;PAGE:STRING:ARTICLE/CHAPTER.

[43] C. Yang, D.G. Yu, D. Pan, X.K. Liu, X. Wang, S.W.A. Bligh, G.R. Williams, Electrospun pH-sensitive core–shell polymer nanocomposites fabricated using a tri-axial process, Acta Biomater 35 (2016) 77–86. https://doi.org/10.1016/J.ACTBIO.2016.02.029.

[44] C.A. Bonino, K. Efimenko, S.I. Jeong, M.D. Krebs, E. Alsberg, S.A. Khan, Three-dimensional electrospun alginate nanofiber mats via tailored charge repulsions, Small 8 (2012) 1928–1936. https://doi.org/10.1002/SMLL.201101791;WGROUP:STRING:PUBLICATION.

[45] K. Saito, T. Xu, H. Ishikita, Correlation between C•O Stretching Vibrational Frequency and p KaShift of Carboxylic Acids, Journal of Physical Chemistry B

126 (2022) 4999–5006. https://doi.org/10.1021/ACS.JPCB.2C02193/ASSET/IMAGES/LARGE/JP2C02193_0009.JPEG.

[46] M. Nara, H. Morii, M. Tanokura, Coordination to divalent cations by calcium-binding proteins studied by FTIR spectroscopy, Biochimica et Biophysica Acta (BBA) - Biomembranes 1828 (2013) 2319–2327. https://doi.org/10.1016/J.BBAMEM.2012.11.025.

[47] F. Takalani, P. Kumar, P.P.D. Kondiah, Y.E. Choonara, Co-emulsified Alginate-Eudragit Nanoparticles: Potential Carriers for Localized and Time-defined Release of Tenofovir in the Female Genital Tract, AAPS PharmSciTech 25 (2024) 1–17. https://doi.org/10.1208/S12249-023-02723-4/FIGURES/8.

[48] Y. Wang, Y. Yue, S. Yang, S. Duan, Y. Yang, Z. Wang, X. Li, B. Li, Y. Wang, Preparation of polyvinyl alcohol/pullulan nanofibers and Eudragit® S100/polyvinyl alcohol/pullulan core-shell nanofibers for enhanced probiotic storage and oral viability, Food Hydrocoll 164 (2025) 111172. https://doi.org/10.1016/J.FOODHYD.2025.111172.

[49] A. Nikam, P.R. Sahoo, S. Musale, R.R. Pagar, A.C. Paiva-Santos, P.S. Giram, A Systematic Overview of Eudragit® Based Copolymer for Smart Healthcare, Pharmaceutics 2023, Vol. 15, Page 587 15 (2023) 587. https://doi.org/10.3390/PHARMACEUTICS15020587.

[50] F. Madiyar, L. Suskavcevic, K. Daugherty, A. Weldon, S. Ghate, T. O'Brien, I. Melendez, K. Morgan, S. Boetcher, L. Namilae, Optimizing Production, Characterization, and In Vitro Behavior of Silymarin–Eudragit Electrosprayed Fiber for Anti-Inflammatory Effects: A Chemical Study, Bioengineering 2024, Vol. 11, Page 864 11 (2024) 864. https://doi.org/10.3390/BIOENGINEERING11090864.

[51] M. Ortega-Muñoz, P. Vargas-Navarro, S. Plesselova, M.D. Giron-Gonzalez, G.R. Iglesias, R. Salto-Gonzalez, F. Hernandez-Mateo, A. V. Delgado, F.J. Lopez-Jaramillo, F. Santoyo-Gonzalez, Amphiphilic-like carbon dots as antitumoral drug vehicles and phototherapeutical agents, Mater Chem Front 5 (2021) 8151–8160. https://doi.org/10.1039/D1QM00855B.

[52] L.L. Shevchenko, INFRARED SPECTRA OF SALTS AND COMPLEXES OF CARBOXYLIC ACIDS AND SOME OF THEIR DERIVATIVES, Russian Chemical Reviews 32 (1963) 201. https://doi.org/10.1070/RC1963V032N04ABEH001329.

[53] H. Sahana, D.K. Khajuria, R. Razdan, D.R. Mahapatra, M.R. Bhat, S. Suresh, R.R. Rao, L. Mariappan, Improvement in Bone Properties by Using Risedronate Adsorbed Hydroxyapatite Novel Nanoparticle Based Formulation in a Rat Model of Osteoporosis, J Biomed Nanotechnol 9 (2013) 193–201. https://doi.org/10.1166/JBN.2013.1482.

[54] I. Grigoraviciute-Puroniene, A. Zarkov, K. Tsuru, K. Ishikawa, A. Kareiva, A novel synthetic approach for the calcium hydroxyapatite from the food products,

J Solgel Sci Technol 91 (2019) 63–71. https://doi.org/10.1007/S10971-019-05020-4/FIGURES/9.

[55] V.H.J.M. dos Santos, D. Pontin, G.G.D. Ponzi, A.S. de G. e. Stepanha, R.B. Martel, M.K. Schütz, S.M.O. Einloft, F. Dalla Vecchia, Application of Fourier Transform infrared spectroscopy (FTIR) coupled with multivariate regression for calcium carbonate (CaCO3) quantification in cement, Constr Build Mater 313 (2021) 125413. https://doi.org/10.1016/J.CONBUILDMAT.2021.125413.

[56] M. Amani, A. Rakhshani, S. Maghsoudian, M. Rasoulzadehzali, S. Yoosefi, S. Keihankhadiv, Y. Fatahi, B. Darbasizadeh, S.M. Ebrahimi, N.M. Ejarestaghi, H. Farhadnejad, H. Motasadizadeh, pH-sensitive bilayer electrospun nanofibers based on ethyl cellulose and Eudragit S-100 as a dual delivery system for treatment of the burn wounds; preparation, characterizations, and in-vitro/in-vivo assessment, Int J Biol Macromol 249 (2023) 126705. https://doi.org/10.1016/J.IJBIOMAC.2023.126705.

[57] S. Kakunje, N. Badiadka, S. Balladka Kunhanna, S. Mahammad, Suchitra, R. Punchappady Devasya, D. Bikrodi Sesappa, S. Varija Raghu, Fabrication, Characterization and In Vitro Drug Release Behavior of Electrospun Eudragit/Eugenol Nanofibrous Scaffold, Fibers and Polymers 25 (2024) 2817–2833. https://doi.org/10.1007/S12221-024-00622-4/FIGURES/15.

[58] V.P. Nirwan, M. Lasak, K. Ciepluch, A. Fahmi, Hybrid Nanomat: Copolymer Template CdSe Quantum Dots In Situ Stabilized and Immobilized within Nanofiber Matrix, Nanomaterials 2023, Vol. 13, Page 630 13 (2023) 630. https://doi.org/10.3390/NANO13040630.

[59] V.P. Nirwan, A. Al-Kattan, A. Fahmi, A. V. Kabashin, Fabrication of Stable Nanofiber Matrices for Tissue Engineering via Electrospinning of Bare Laser-Synthesized Au Nanoparticles in Solutions of High Molecular Weight Chitosan, Nanomaterials 2019, Vol. 9, Page 1058 9 (2019) 1058. https://doi.org/10.3390/NANO9081058.

[60] C. Xu, K. Yuan, X. Jin, Z. Yu, L. Zheng, Y. Lü, X. Wang, L. Zhu, G. Zhang, D. Xu, High-temperature stable electrospun MgO nanofibers, formation mechanism and thermal properties, Ceram Int 43 (2017) 16210–16216. https://doi.org/10.1016/J.CERAMINT.2017.08.199.

[61] S. Salmanipour, A. Rezaie, N. Alipour, M. Ghahremani-Nasab, M.S. Zakerhamidi, N. Akbari-Gharalari, A. Mehdipour, R. Salehi, S. Jarolmasjed, Development of Polyphosphate/Nanokaolin-Modified Alginate Sponge by Gas-Foaming and Plasma Glow Discharge Methods for Ultrarapid Hemostasis in Noncompressible Bleeding, ACS Applied Materials and Interfaces 16 (2024) 34684–34704. https://doi.org/10.1021/ACSAMI.4C05695/SUPPL_FILE/AM4C05695_SI_013.MP4.

[62] M. Dargahi, E. Konkov, S. Omanovic, Influence of Surface Charge/Potential of a Gold Electrode on the Adsorptive/Desorptive Behaviour of Fibrinogen, Electrochim Acta 174 (2015) 1009–1016. https://doi.org/10.1016/J.ELECTACTA.2015.06.065.

[63] V. Deineka, O. Sulaieva, N. Pernakov, J. Radwan-Pragłowska, L. Janus, V. Korniienko, Y. Husak, A. Yanovska, I. Liubchak, A. Yusupova, M. Piątkowski, A. Zlatska, M. Pogorielov, Hemostatic performance and biocompatibility of chitosan-based agents in experimental parenchymal bleeding, Materials Science and Engineering: C 120 (2021) 111740. https://doi.org/10.1016/J.MSEC.2020.111740.

[64] Q. Yu, B. Su, W. Zhao, C. Zhao, Janus Self-Propelled Chitosan-Based Hydrogel Spheres for Rapid Bleeding Control, Advanced Science 10 (2023) 2205989. https://doi.org/10.1002/ADVS.202205989.

[65] J.W. Weisel, R.I. Litvinov, Red blood cells: the forgotten player in hemostasis and thrombosis, Journal of Thrombosis and Haemostasis 17 (2019) 271–282. https://doi.org/10.1111/JTH.14360.

[66] S. Raghunathan, J. Rayes, A. Sen Gupta, Platelet-inspired nanomedicine in hemostasis thrombosis and thromboinflammation, Journal of Thrombosis and Haemostasis 20 (2022) 1535–1549. https://doi.org/10.1111/JTH.15734/ASSET/12BCA200-D785-49EC-8FD6-F4394C8D8097/MAIN.ASSETS/JTH15734-FIG-0004-M.JPG.

[67] T.U. Habibah, D. V. Amlani, M. Brizuela, Hydroxyapatite Dental Material, StatPearls (2022). https://www.ncbi.nlm.nih.gov/books/NBK513314/ (accessed July 2, 2025).

[68] N. Li, G. Zhang, Y. Liu, L. Sun, X. Zhao, L. Ding, Y. Liu, M. Wang, X. Ren, A Natural Self-Assembled Gel-Sponge with Hierarchical Porous Structure for Rapid Hemostasis and Antibacterial, Adv Healthc Mater 12 (2023) 2301465. https://doi.org/10.1002/ADHM.202301465;WEBSITE:WEBSITE:ADVANCED;CTYPE:STRING:JOURNAL.

[69] Q. Xu, E. Hu, H. Qiu, L. Liu, Q. Li, B. Lu, K. Yu, F. Lu, R. Xie, G. Lan, Y. Zhang, Catechol-chitosan/carboxymethylated cotton-based Janus hemostatic patch for rapid hemostasis in coagulopathy, Carbohydr Polym 315 (2023) 120967. https://doi.org/10.1016/J.CARBPOL.2023.120967.

[70] K. Quan, G. Li, L. Tao, Q. Xie, Q. Yuan, X. Wang, Diaminopropionic Acid Reinforced Graphene Sponge and Its Use for Hemostasis, ACS Appl Mater Interfaces 8 (2016) 7666–7673. https://doi.org/10.1021/ACSAMI.5B12715/ASSET/IMAGES/MEDIUM/AM-2015-127159_0005.GIF.

[71] Z. Chen, X. Yao, L. Liu, J. Guan, M. Liu, Z. Li, J. Yang, S. Huang, J. Wu, F. Tian, M. Jing, Blood coagulation evaluation of N-alkylated chitosan, Carbohydr Polym 173 (2017) 259–268. https://doi.org/10.1016/J.CARBPOL.2017.05.085.

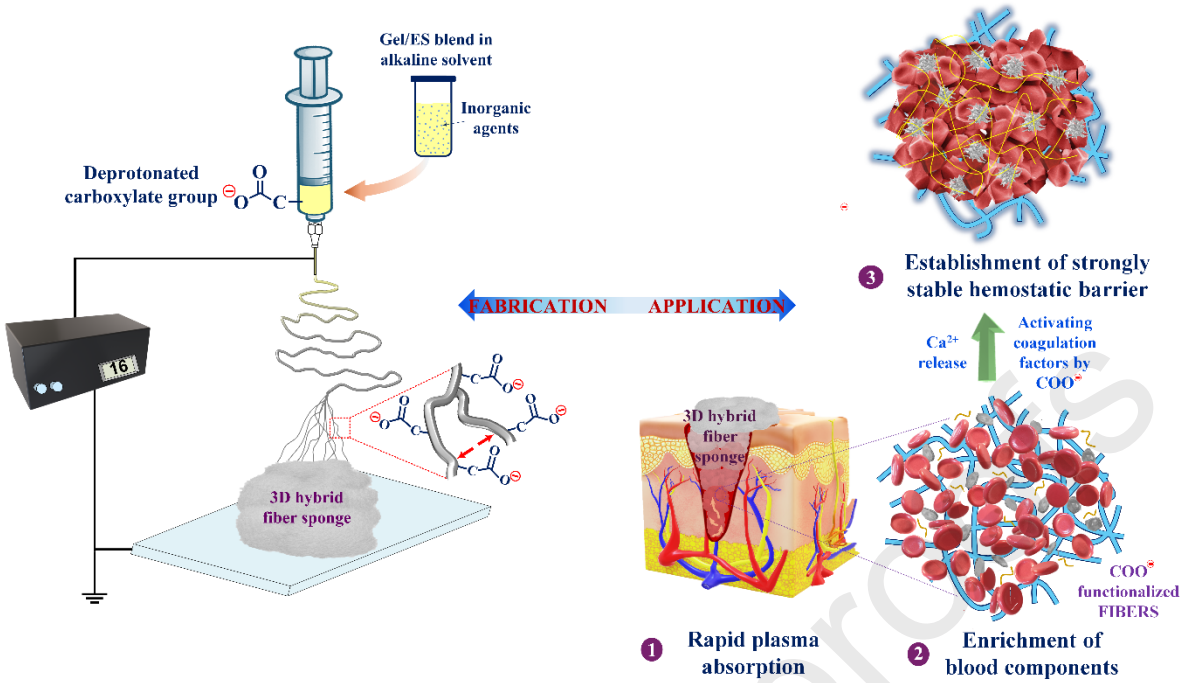

- A facile strategy for deprotonated carboxylate-assisted direct electrospinning of fluffy fiber sponge was reported for the first time.
- Deprotonated carboxylate simultaneously imparts three-dimensionality, superhydrophilicity, and highly negatively charged surfaces to fibrous matrices.
- Hybrid fiber could facilitate the adherence and aggregation of abundant blood cells, forming an impermeable barrier.
- 3D hybrid fiber sponge shows superior hemostasis performance than traditional alternatives.